AIRFRAME/PROPULSION INTEGRATION CHARACTERISTICS AT TRANSONIC SPEEDS

William P. Henderson and Bobby L. Berrier
NASA Langley Research Center
Hampton, Virginia

ABSTRACT

The aerodynamic characteristics for both single and twin-engine high-performance aircraft are significantly affected by shock induced flow interactions as well as other local flow interference effects which usually occur at transonic speeds. These adverse interactions can not only cause high drag, but also cause unusual aerodynamic loadings and/or severe stability and control problems. Many new programs are under way to not only develop methods for reducing the adverse effects, but also to develop an understanding of the basic flow conditions which are the primary contributors. It is anticipated that these new programs will result in technologies which can reduce the aircraft cruise drag through improved integration as well as increase aircraft maneuverability through the application of thrust vectoring. This paper will attempt to identify some of the primary integration problems for twin-engine aircraft at transonic speeds, and demonstrate several methods for reducing or eliminating the undesirable characteristics, while enhancing configuration effectiveness.

NOMENCLATURE

C_D	Total afterbody drag coefficient
C_{Dtail}	Drag coefficient of the tail surfaces (tail drag + interference)
C_{D_n}	Nozzle drag coefficient
ΔC_D	Incremental drag coefficient
C_m	Pitching moment coefficient
C_n	Yawing moment coefficient
C_p	Pressure coefficient
F/F_i	Ratio of thrust to ideal thrust
F_r/F_i	Ratio of resultant (gross) thrust to ideal thrust
H_T	Horizontal tail
ℓ	Length of model

M	Mach number
NPR	Nozzle pressure ratio
q	Dynamic pressure
VT	Vertical tail
X	Distance from nose of model to pressure orifice
α	Angle of attack
β	Nozzle boattail angle
$\beta_{side}/\beta_{flap}$	Ratio of boattail angle of sidewalls to boattail angle of nozzle upper and lower flaps
δ_y	Flow turning angle
$\delta_{y,i}$	Ideal flow turning angle
$\delta_{v,p}$	Deflection of the nozzle upper and lower flaps
ϕ	Roll angle location of pressure measuring devices
θ	Nozzle cant angle

Abbreviations:

AFT	Rear location
Axi	Axisymmetric
Fwd	Forward location
L.E.	Leading edge
Mid	Middle location
Non axi	Nonaxisymmetric
SMTD	STOL and Maneuver Technology Demonstrator

INTRODUCTION

The mission requirements for the next generation fighter aircraft may dictate a highly versatile vehicle capable of operating over a wide range of flight conditions. This aircraft will most likely be designed for high maneuverability and agility, operate in a highly hostile environment, and possess STOL landing characteristics to operate from bomb damaged airfields (reference 1). Many design guidelines tend to be contradictory for the

subsonic and supersonic speed regimes and aircraft performance can be compromised by small changes in these design considerations.

The attainment of high performance is highly dependent upon the minimization of interference resulting from the integration of the propulsion exhaust system into the airframe, one of the most critical design features of an aircraft (reference 2). An indication of the relative importance of this area is illustrated in figure 1 where the percent of total aircraft drag attributed to the aircraft afterbody is presented for four twin-engine fighter aircraft. Representative aircraft from an "ideal" research configuration tested in 1961 to the F-18 aircraft tested in 1978 are shown. The afterbodies of these models comprised from 20 to 35 percent of the total model length, but produced 38 to 50 percent of the total aircraft drag. Up to half of the afterbody drag results from adverse interference in the afterbody region and pressure drag on the afterbody (see reference 3-6).

At the same time the designer is striving for a low drag configuration, he is also required to improve the maneuvering capability of the aircraft. This usually requires high thrust to weight and lift drag ratio, high usable lift coefficient, and adequate stability and control characteristics over a very wide operating envelope.

In responding to the need to reduce nozzle/afterbody drag and enhance vehicle maneuverability, the Propulsion Aerodynamics Branch at the Langley Research Center has conducted a number of responsive experimental and theoretical research programs. In these programs, items such as empennage location and nozzle boattail geometry have been investigated. Increasing maneuverability, particularly at post stall conditions where conventional controls are ineffective, requires the utilization of alternative control devices. One of the most effective, particularly at high angles of attack, relies on vectoring of the engine thrust. As indicated, the empennage is a source of high interference drag. Therefore, reducing the size of the empennage or eliminating it altogether would increase aircraft performance, but could cause serious problems for aircraft stability and control. Thrust vectoring can be a means to provide the necessary control power, or at least augment it. This means that effective thrust vectoring must be provided across the aircraft speed regime. Various concepts have been studied (see references 7 and 8) at transonic speeds and typical results will be discussed herein.

WIND TUNNEL

All of the experimental investigations discussed herein were conducted in the Langley 16-Foot Transonic Tunnel. This tunnel is a continuous flow, single-return, atmospheric wind tunnel with a slotted octagonal throat and test section, and continuous air exchange. The tunnel has a variable speed range from $M = 0.20$ to $M = 1.30$. Additional information regarding tunnel description and calibration is presented in reference 9.

DISCUSSION

Nozzle/Afterbody Integration

In an analysis of this type, where the integration characteristics of twin-engine high-performance aircraft are being studied, it is important to develop an understanding of the contribution of the various nozzle/afterbody components to the total aircraft drag. The model used in conducting this analysis is presented in figure 2.

The centerbody fuselage of this model was essentially rectangular in cross section having a constant width and height of 10.0 in. and 5.0 in. respectively. The four corners were rounded by a radius of 1.0 in. Maximum cross-sectional area of the centerbody (fuselage) was 49.14 in^2. The support system forebody was typical of a powered model in that the inlets were faired over. The "wings" of the support system were mounted above the model centerline in a "high wing" position which is typical of many current fighter designs. The support system "wing" had a 45° leading edge sweep, a taper ratio of 0.5, an aspect ratio of 2.4, and a cranked trailing edge. The airfoil was symmetrical and the thickness ratios near the wing fuselage junction were realistic (approximately t/c = 0.067). From BL 11.00 to the support booms, however, "wing" thickness ratio increased from t/c = 0.077 to t/c = 0.10 to provide structural support for the model and to permit transfer of compressed air from the booms to the model propulsion system.

The twin-engine aft-end was attached to the support system wing/centerbody by mounting on a six-component strain gage balance. The combined forces and moments for the afterbody shell, empennage surfaces, and outer nozzles were measured by the balance and are termed total aft-end forces in this paper. Clearance was provided between the metric and nonmetric portions of the model. The afterbody lines were chosen to be typical of current close-spaced twin-engine fighter designs, to fair the afterbody smoothly from the constant cross section of the centerbody down to the nozzles, and to house the afterbody balance, propulsion simulation system, and related instrumentation. Nozzle geometry simulated a convergent-divergent nozzle design with fully variable throat area and expansion ratio.

The contribution of the various nozzle/afterbody components to the total afterbody drag is presented in figures 3 to 5. This drag breakdown (taken from data in reference 10) is for the twin-engine configuration with dry power axisymmetric nozzles at a scheduled nozzle pressure ratio (NPR). Scheduled nozzle pressure ratio for the various test mach numbers is as follows:

M	NPR
0.60	3.5
.80	4.5
.90	5.0
.95	5.3
1.15	6.7
1.20	7.0

The circular symbols in figure 3 represent the drag data for the complete afterbody configuration and the square symbols for the nozzle/afterbody configuration without horizontal or vertical tails. An estimate shown by the dashed line was made of the drag increment attributed by the horizontal and vertical tails. This increment represents the skin friction and form drag at subsonic speeds and the skin friction and wave drag at supersonic speeds. The difference in drag between the dashed line and the total drag can be attributed to an adverse interference effect. This adverse drag increment is small at M = 0.60 but increases dramatically as the Mach number approachs 0.95. From this curve it is obvious that the horizontal and vertical tails and their associated adverse interference effects are the major contributors to the nozzle/afterbody drag. This is better illustrated in figure 4 where the drag contribution of the tail surfaces (tail drag + interference effects) is presented as a function of the total afterbody drag for several configurations. As shown in this figure, the horizontal and vertical tails contribute as much as 60 to 70 percent of the nozzle/afterbody drag, and as shown in figure 3 at transonic speeds, about half of this drag can result from adverse interference effects.

Exploring the drag contribution of the various model components in a little more detail can be accomplished with the aid of figure 5. The square symbols in this figure, nozzle/afterbody drag (horizontal and vertical tails off) are the same as the data shown on figure 3. The diamond symbols represent the data for the nozzle alone. These data include the pressure drag obtained by integrating the nozzle static pressures and an estimated skin friction drag. An estimate was made of the friction drag of the afterbody, and this is shown added to the nozzle drag as the solid line. The remaining drag is attributed to the pressure drag on the afterbody which is seen to be about 20 drag counts at subsonic speeds and about 60 drag counts at supersonic speeds. Possibly, with some careful contouring and the elimination of the gutters between the engine, this drag increment can be reduced. From these data it would appear that the two major areas for increasing the performance (decreasing the drag) of a typical afterbody configuration are in the elimination of the interference drag associated with the horizontal and vertical tails and reducing the pressure drag associated with the afterbody.

Nonaxisymmetric Nozzles

For a number of years, the Langley Research Center has recognized that there are a number of advantages to the application of nonaxisymmetric nozzles in place of the current axisymmetric nozzles. Some of these benefits are indicated in reference 11. One of these benefits is the possible reduction in nozzle/afterbody drag due to a better integration of the afterbody. A number of configurations have been studied; one of these mounted in the 16-Foot Transonic Tunnel is shown in figure 6. The wings and forebody are the same as those of the previous model with the axisymmetric nozzle. Only the aft portion of the model (aft of the metric break) has been changed. The metric portion of the model consisted of the internal propulsion system, afterbody, tails, and nozzles. The afterbody lines (boattail) were chosen to provide a length of constant cross-section aft of the nonmetric centerbody, and to enclose the force balance and jet simulation system, while fairing smoothly downstream into the closely spaced nozzles. The afterbody shell and tail surfaces were attached to an afterbody force balance which was attached to the main force balance. The main force balance in turn was grounded to the

nonmetric wing-centerbody section. The nozzles were attached directly to the main force balance through the propulsion system piping.

The nonaxisymmetric (two-dimensional convergent-divergent) nozzle used in this investigation simulated a dry-power or cruise operating nozzle with a design NPR of about 3.5. The nozzle throat area (17.48 cm^2) and expansion ratio (1.15) were sized to be consistent with advanced mixed flow turbofan cycles. The ratio of total throat area to maximum body cross-sectional area was 0.11, and the nozzle throat aspect ratio was 3.45.

The experimental drag characteristics for this configuration (taken from reference 12) are shown compared to the configuration with axisymmetric nozzles in figures 7 and 8. In figure 7, the drag characteristics for the complete afterbody (tails on) configurations are presented. The drag characteristics for the configurations without the horizontal and vertical tails are presented in figure 8. At the lower test Mach numbers, the configuration (tails-on) with the nonaxisymmetric nozzles has the lowest drag. As the Mach number is increased, this trend changes and the drag for the configuration with the axisymmetric nozzles is significantly lower. For the tails off configurations, the configuration with the nonaxisymmetric nozzles has the lowest drag at mach numbers up to 0.90. This would seem to indicate that the nonaxisymmetric nozzle concept may be more sensitive to adverse tail interference effects than the axisymmetric nozzles at the Mach numbers where these effects are generally very high. At supersonic speeds, nozzle drag is significantly higher for the nonaxisymmetric nozzle, which means that some changes in the nozzle geometry and area distribution may have to be made in order to reduce drag.

Nozzle Boattail Drag Effects

A number of studies on methods of reducing the drag on nonaxisymmetic nozzles have been conducted. One such study, aimed at determining the effects of nozzle boattail geometry on the nozzle drag, is illustrated by several typical models which are shown in figures 9 and 10. The only difference between these two models is in the nozzle geometry; a 7.5° boattail nozzle is shown in figure 9 and a 12.5° boattail nozzle is shown in figure 10. The nozzle drag characteristics (taken from reference 13) presented as a function of boattail angle is shown in figure 11. The nozzle boattail angle for the model previously shown in figure 6 was about 17°. Based on these data, some significant drag reductions could be obtained with a small reduction in boattail angle. This of course would have to be traded against a potential weight increase usually associated with reducing boattail angle.

Most of the nonaxisymmetric nozzle designs that have been previously studied have taken almost all of the nozzle boattail on the top and bottom surfaces of the nozzle, leaving the sidewalls nearly flat. During earlier tests, where surface pressures were measured on the external surfaces of the nozzle, some significant difference in pressure distributions was noted. Pressure distributions on the upper and lower nozzle surfaces were much lower than pressure distributions on the nozzle sidewalls. It was felt that this difference would cause some cross flow around the nozzle creating a potential drag problem. As a result, a study was devised with the General Dynamics Corporation to measure the nozzle/afterbody drag for a configuration in which

the nozzle upper and lower surface boattail angles are traded against the sidewall boattail angle. The sketch of the model used in this study (taken from reference 14) is shown in figure 12, and the nozzle/afterbody drag coefficient variation as a function of the ratio $\beta_{side}/\beta_{flap}$ for Mach numbers of 0.90 and 1.20 is presented in figure 13. The boattail angles for the nozzle upper and lower flaps and the sidewalls that correspond to the ratios presented in figures 12 and 13 are as follows:

$\beta_{side}/\beta_{flap}$	β_{flap}, deg	β_{side}, deg
0.50	15.0	7.5
1.00	13.5	13.5
1.77	11.0	19.5

The results of this study indicate that minimum nozzle/afterbody drag occurs when the boattail angles on all of the surfaces are approximately the same. It should also be noted that for $\beta_{side}/\beta_{flap} = 1.0$, the boattail angles are 13.5° which, according to figure 11, may be near the most optimum boattail angle for nonaxisymmetric nozzles at M = 0.90. The drag coefficient increases more rapidly as the ratio $\beta_{side}/\beta_{flap}$ decreases below 1.0 than when it increases above 1.0. This occurs because as $\beta_{side}/\beta_{flap}$ decreases, the upper and lower flap boattail angle increases while the sidewall boattail angles decreases. Since the upper and lower flap are considerably larger than the sidewall flaps, any adverse drag effects on the upper and lower flaps would be more significant than any potential decreases on the small sidewall flaps.

Effect of Empennage Location

While there are some significant benefits that can be realized with changes in the geometry of the nozzle/afterbody, the largest drag penalty at transonic speeds according to figure 3 was attributed to the horizontal and vertical tails. Several studies have been conducted to determine the effects of horizontal and vertical tail locations on the nozzle/afterbody drag. The results of these studies are summarized in figures 14, 15, and 16 and were taken from reference 10 for the configuration with axisymmetric nozzles and from reference 12 for the configurations with nonaxisymmetric nozzles (see figure 6). The afterbody had provisions for mounting both the vertical and horizontal tails in three axial locations as illustrated in figure 14. Note that the leading edge of the root chords for both horizontal and vertical tails could be placed at the same fuselage axial station. These locations will be termed fwd, mid, and aft respectively.

The effects of horizontal and vertical tail location on the nozzle drag are shown in figure 15 for dry power nozzles at $\alpha = 0^0$ and Mach numbers of 0.90 and 1.20. The open symbols are for the configuration with axisymmetric nozzles and the solid symbols are for the configuration with nonaxisymmetric nozzles. Moving either the horizontal or vertical tails from the aft position (location closest to the nozzle) to the mid position results in a significant reduction in the nozzle drag. Further movement of the tails away from the nozzles had only a minor effect on the nozzle drag. However, when you look at the total aftend drag, the results are not so clear. In figure 16, the total

nozzle/afterbody drag is presented as a function of horizontal and vertical tail location. While a slight drag reduction trend can be deduced as the tails are moved away from the nozzles, there are still some configurations that show opposite effects. This would seem to indicate that as the tails are moved away from the nozzles on these twin-engine configurations, the adverse tail interference effects on nozzles are transferred to the afterbody. Thus, it would appear that there may be only two ways that can be utilized to eliminate this large adverse interference effect. One is to simply eliminate the ho ontal and vertical tails and utilize some other method of achieving the necessary control power. The other is to develop an adequate computational method which can be utilized to carefully contour the nozzle/afterbody thereby eliminating the adverse interference effects.

Computational Methods

Several computational methods are being developed that can be utilized in solving this complex nozzle/afterbody/empennage integration problem. One of these is a full-potential finite-volume transonic code called FLO-30V (reference 15), which is used to calculate the pressure distributions over the nozzle/afterbody including the effects of the empennage. In this code an integral boundary-layer calculation is performed in strip fashion. The resulting effective body and tail geometries are used as input to the code. This developmental code utilizes the method of Caughey and Jameson which is based upon the full potential equation and a mesh generation technique which wraps a C-type grid around the body and tails. Further discussion of the methods used in these calculations and of the comparisons of calculations with experimental data can be found in reference 16.

This code was applied to the sting-strut supported single-engine model which is presented in figure 17. This type of support system places the model centerline on the centerline of the wind tunnel and minimizes support interference on the afterbody and nozzle. The overall model arrangement, representing a typical single-engine fighter aft end, is composed of four major parts located as shown in the following table:

Part	x,in.	x/l
Forebody	0-40.89	0-0.57
Afterbody	40.89-64.89	0.57-0.91
Nozzle	64.89-71.70	0.91-1.00
Tail surfaces	Variable	Variable

The forebody consists of an ogive nose 24 inches in length with an initial angle of 14° and a constant-radius cylinder thereafter. The afterbody was designed to simulate closure ahead of the nozzle typical of a single-engine fighter configuration. The afterbody had provisions for mounting the vertical and horizontal tails at two different axial locations (forward and aft). The tail surfaces were tested in three empennage arrangements: aft, staggered, and forward. The nozzle used for this investigation simulated a variable geometry (fixed in dry power mode for this test), convergent-divergent, axisymmetric nozzle typical of those currently in use on modern

fighter aircraft. A complete description of the model is given in reference 16.

An assessment of the effectiveness of the Flo30V code at predicting the nozzle/afterbody/empennage pressures can be made with the aid of the comparisons presented in figures 18 and 19. A comparison of the theoretical calculations with experimental data for two rows of pressure orifices on the staggered empennage arrangement, one near the vertical tail at a roll angle of 18° and the other near the horizontal tail at a roll angle of 72°, is presented in figure 18 for a Mach number of 0.60 and for a Mach number of 0.90 in figure 19. The staggered tail arrangment was chosen for these comparisons because the data indicated that for the single-engine configuration, the empennage interference effects were lowests for this tail arrangement. The calculated results show reasonably good agreement with the experimental data at the lowest test Mach number (M = 0.60). At the higher subsonic test Mach numbers (M = 0.90), the discrepancy between the experiment and theory becomes more significant. The major reason for the discrepancy could probably be attributed to the approximations made to model the vertical tail and the lack of a model of the wake of the vertical tail. The FLO-30V calculations do account for viscous effects, but the boundary layers on the body and tail were computed separately as two-dimensional elements, so that the influence of the empennage is not included in the afterbody boundary-layer calculations. As a result, the FLO-30V calculation shows some influence of the empennage on nozzle/afterbody pressures, but does not predict the severity of the interference effects.

Thrust Vectoring

As indicated previously, one of the most efficient ways of reducing the adverse interference drag caused by the horizontal and vertical tails is to simply remove them from the configuration. This could be accomplished if some other method were found to provide the necessary control power for the configuration. One of the obvious solutions would be to rely on thrust vectoring to fill this void. Thrust vectoring has been studied for some time and has been found to provide a number of potential enhancements to aircraft performance and effectiveness. Many of these are indicated in the following:

Increased Capabilities
- STOL
- Expanded envelope

Improved Performance
- Control Augmentation
  - Post stall operation
  - Higher instantaneous turn rates
  - Fuselage aiming
  - Direct force control
- Lower Drag
  - Reduced trim drag
  - Reduced control surface drag

- Lower Weight
  - Elimination of control surfaces
- Less Design Constraints
  - Supersonic wing design
  - Low q control surface sizing

Improved Survivability

Methods of providing pitch vectoring have been under study for some time, (see reference 8). These studies have shown that many nozzles can be designed to provide high levels of pitch vectoring without a significant adverse impact on aircraft thrust performance. The challenge now becomes one of providing, in addition to the pitch vectoring, a high level of yaw vectoring. A number of configurational concepts have been studied. Some of these, shown in figure 20, were based on configurations studied in references 17 and 18.

The upstream yaw vectoring concept was achieved by modifying one of the nozzle sidewalls with a rectangular port located upstream of the nozzle throat. The port was sized to have an area equal to 30 percent of the unvectored dry power nozzle throat area. The port operates by deflecting two flaps. The forward flap was a simple flap hinged at the nozzle sidewall and extended into the external flow. The aft flap was also hinged at the nozzle sidewall, but it deflected both into the external flow as well as into the internal flow (about 45 percent of the internal nozzle width). These flaps were deflected at an angle of about 70° to the axial thrust direction.

The downstream (of throat) yaw vectoring concept (sidewall flaps) is based on modifying either the left or right sidewall or both sidewalls with a hinged flap extending downstream of the nozzle throat. The sidewall flaps hinged directly at the nozzle throat. Consequently, for a positive yaw vector angle (produces positive side force), the left sidewall flap extends out from the internal nozzle flow (expansion turn), while the right sidewall flap extended into the flow (compression turn). This type of concept does have some limitations in that there could be some interference between surfaces when simultaneous pitch and yaw vectoring are required.

The third concept consisted of externally mounted vanes, one on each side of the nozzle. The vanes hinged at the nozzle exit are deflected such that one vane extends into the jet exhaust flow whereas the other extends away from the jet exhaust flow. The height of the vanes was determined by the location of the nozzle when pitch vectoring is included. For a ±15° nozzle pitch vector angle, the lower (or upper) trailing edge of the nozzle coincides with the lower (or upper) edge of the vane.

The static yaw vectoring results for these three concepts are presented in figure 21. On the left side of the figure, the measured yaw vector angle determined from static tests in the Langley Static Test Stand is presented. On the right side is the ratio of the measured yaw vector angle to the expected yaw vector angle (determined geometrically from the known deflection angles of the surfaces involved).

The results indicate that the rectangular port concept produced a high yaw vector (turning) angle, about the magnitude anticipated (based on $\delta_y/\delta_{y,i} = 1.0$). This level of vectoring would be expected since the exhaust flow upstream of the nozzle throat is subsonic and past experience has shown that subsonic flow can be turned with only very small losses. The data for the sidewall flaps show significant variation in yaw vector angle with nozzle pressure ratio. At the lower NPR's the flow is probably separated off of the deflected flap on the expansion side (flap deflected away from the jet exhaust). As the nozzle pressure ratio increases, the flow tends to expand around the flap and the vector angle increases. The full potential of the yaw vector angle is probably not reached simply because the entire jet exhaust is not affected by the small sidewall flaps. The post-exit vanes produce the smallest level of yaw vectoring of any of the vectoring concepts studied at these static conditions. For this concept, the flow over the vane that was deflected away from the jet exhaust was totally separated. Therefore, it was totally ineffective at producing any contribution to yaw vectoring at all nozzle pressure ratios. In this case only the vane extending into the flow produced any yaw vectoring and it had to turn a supersonic exhaust stream which from past experience is very inefficient.

The external flow effects on the yaw vectoring produced by these three concepts are shown in figures 22 through 24. In these figures, the yawing moment multiplied by free-stream dynamic pressure is presented as a function of Mach number. It should be noted that for presentation purposes, the sign on yawing moment was changed from negative values (which would result from the positive flap deflections shown in figure 20) to positive values (which would result from negative flap deflections). On each of these figures, three pieces of data are presented. The circular symbols are the yawing moment based on the direct thrust contribution. These data were obtained from the yawing moment measured at static (wind-off) conditions multiplied by the ratio of the free stream static to the free stream dynamic pressure. The shaded area is the aerodynamic contribution of the vectoring device to the yawing moment measured by conducting the experimental test at jet-off conditions with external flow. The square symbols are the measured yawing moment at jet on conditions with external flow. The arrows shown in figures 22 to 24 indicate an induced external flow contribution to yawing moment caused by any interaction of the external flow with the jet-on vectored exhaust plume and any surrounding model surfaces. For the three cases presented in figures 22 through 24, the jet nozzle pressure ratio is 3.0. The yawing moment as a function of Mach number is presented for the upstream port in figure 22, for the sidwall flaps in figure 23, and for the post exit vanes in figure 24. For the upstream rectangular port configuration, the small flaps protruding from the side of the nozzles results in a small positive increment (aero. flap effect) in yawing moment which increases as the Mach number increases. The induced external flow contribution at jet on conditions, illustrated by the arrows, indicate that the external flow has an adverse contribution to the yawing moment. It is thought that this adverse effect could either be caused by the external flow altering the angle of the jet plume as it eminates from the side of the nozzle or by creating large negative pressures on the sidewall behind the jet plume. For the sidewall flap configuration (see figure 23), both the flaps themselves and the induced external flow contributions produced a positive increment in yawing moment. The increments are relatively small, which is expected since the flaps are small, and the deflection angle is only

20°. The largest external flow effects show up on the post-exit vane configuration (see figure 24). As shown, increasing Mach number causes large increases in the yawing moment obtained. The major portion of this increase is the result of a jet off aerodynamic effect on the vanes themselves. This is to be expected since the vanes are fairly large and protrude into the airflow, acting essentially like a vertical tail.

A summary of the thrust characteristics of these three yaw vector concepts at static conditions is presented in figure 25. On the left side of the figure, the ratio F/F_i which is the measured thrust along the body axis divided by the ideal thrust is presented. For thrust vectored configurations (symbols), reductions in this ratio from 1.0 are caused by the four following mechanisms: 1) skin friction, internal flow separation and exhaust flow divergence losses, 2) under- and over-expansion losses, 3) turning of the gross thrust vector away from the axial direction and 4) additional skin friction and pressure losses caused by the deployed thrust vectoring hardware and the actual turning process itself. The unvectored baseline configuration (dashed line) is affected by the first two mechanisms only. On the right side of the figure, resultant thrust ratio F_r/F_i is presented as a function of nozzle pressure ratio. This parameter eliminates the losses due to turning the gross thrust vector away from the axial direction (mechanism 3.) Thus, any differences between F_r/F_i for the baseline configuration and F_r/F_i for the vectored configurations are caused by additional losses due to the thrust vector hardware and the turning process itself (mechanism 4). Resultant thrust ratios for the sidewall flap configuration are very close to those of the baseline configuration. This result indicates that little or no additional losses occur due to turning the exhaust flow for this yaw vector concept. Similar results to these have been measured for pitch vector concepts which use upper and lower flaps to obtain a pitch vectoring capability. The post-exit vane configuration had 4 to 6 percent lower resultant thrust ratio than the baseline configuration. Lower performance for this configuration probably results from supersonic exhaust flow separation (on the vane deflected away from the exhaust) and additional skin friction drag on the vanes. The results for the upstream rectangular port configuration show extremely large resultant thrust ratio losses. This loss is not surprising since about 30 percent of the flow did not pass through the main nozzle throat and thus was not efficiently expanded by the nozzle divergent flaps. In addition, this concept probably also has additional separation losses from the backside of the aft flap which extends into the internal exhaust stream.

One disadvantage of the multiplane vectoring concepts is that they require additional mechanism (flap surface or other geometry) to achieve both pitch and yaw thrust vectoring. This is undesirable because of the added weight and complexity. One method of reducing some of this complexity is to utilize twin canted nozzles (see reference 7). This concept is shown in figure 26 and a close-up of the nozzles in is shown in figure 27. Canting of the nozzles is generally accomplished by rotating each of the nozzles about their respective thrust axis. With the nozzles canted, pitching moment is obtained by symmetric nozzle pitch vectoring whereas yawing moment is produced from asymmetric nozzle pitch vectoring. The advantage of this concept is that a pitch vectoring nonaxisymmetric nozzle can be utilized without having to modify the nozzle to accommodate additional mechanisms to obtain yaw vectoring capability.

The variation of pitching and yawing moment coefficients with angle-of-attack are shown in figure 28 at M = 0.20 and NPR = 3.2. These results show that the increment in either C_m or C_n due to varying the nozzle flap deflection angle is constant over the angle-of-attack range tested. Pure pitching moment (no yaw) was obtained by a +20° deflection of the flaps on both nozzles (square symbols on left side of figure 28). Pure yawing moment (no pitch) was obtained by a +20° deflection of the right hand nozzle flaps and a -20° deflection of the left hand nozzle flaps (square symbols on right side of figure 28). Although not shown here, there was no effect of sideslip on C_n over the angle-of-attack range tested. Also shown in figure 28 are the effects of a simultaneous pitch/yaw combination obtained by deflecting the left nozzle 0° and the right nozzle 20°. This is equivalent to 10° of pitch thrust vectoring to obtain pitching moment or ±10° of differential pitch thrust vectoring to obtain yawing moment. For example, the pitching moment coefficient level shown for $\delta_{v,p} = 0^0/20^0$ was essentially equal to that measured for $\delta_{v,p} = 10^0$ (not shown). This result again illustrates that there is generally no coupling of the longitudinal and lateral control moments when using powered controls.

The effect of canting the nozzles on the nozzle/afterbody drag is presented in figure 29. Shown in this figure is an increment in drag coefficient which is defined as the difference in drag for the configuration with a nozzle cant angle of 30° and the same configuration with a cant angle of zero, plotted as a function of Mach number. As shown in figure 29, there is a drag reduction associated with canting the nozzles which at transonic speeds becomes very significant. It is felt that the primary cause for the drag reduction is that the gully between the engines has been nearly eliminated on the lower surface of the afterbody and opened up on the upper surface (see figure 27). There may be some difference in cross-sectional area, but this information has not been developed.

An example of a potential integration of the canted nozzle into the F-15 STOL and maneuver aircraft is shown in figures 30 and 31. For this integration concept, not only the pitch and yaw vectoring advantages are obtained, but the installation of a thrust reverser can be more efficient. For example, on the aircraft under surface, the reverser exhaust is deflected outwards possibly reducing the inlet hot gas reingestion problem and on the upper surface, the reverser exhaust is deflected away from the vertical tails possibly easing some adverse inteference problems.

CONCLUSIONS

A significant research program is ongoing in Langley's Propulsion Aerodynamics Branch on integrating the propulsion system into nigh performance aircraft concepts. This program has included nozzle design, nozzle/afterbody integration, empennage integration, and multiplane vectoring studies. The results of some of those studies presented in this paper are as follows:

1. A significant portion of the afterbody drag is due to the horizontal and vertical tails.

2. Nonaxisymmetric nozzles are competitive with axisymmetric nozzles.

3. Computational methods can provide necessary guidance in propulsion integration.

4. Thrust vectoring concepts are effective in providing combined pitch and yawing moments.

REFERENCES

1. Fletcher, J.; and Burns, B.R.A.: "Supersonic Combat Aircraft Design," AIAA Paper No. 79-0699, March 1979.

2. Nichols, Mark R., "Aerodynamics of Airframe-Engine Integration of Supersonic Aircraft," TN D-3390, 1966, NASA.

3. Corson, Blake W., Jr.; and Runckel, Jack F.: "Exploratory Studies of Aircraft Afterbody and Exhaust-Nozzle Interaction," TM X-1925, 1969, NASA.

4. Runckel, Jack F.: "Interference Between Exhaust System and Afterbody of Twin-Engine Fuselage Configurations," TN D-7525, 1974, NASA.

5. Glasgow, E. R.; and Santman, D. M.: "Aft-End Design Criteria and Performance Prediction Methods Applicable to Air Superiority Fighters Having Twin Buried Engines and Dual Nozzles," AIAA Paper No. 72-1111, Nov.-Dec. 1972.

6. Glasgow, E. R.: "Integrated Airframe-Nozzle Performance for Designing Twin-Engine Fighters," AIAA Paper No. 73-1303, November 1973.

7. Capone, Francis J.; and Mason, Mary L.: Multiaxis Aircraft Contol Power from Thrust Vectoring at High Angles of Attack. NASA Technical Memorandum 87741, June 1986.

8. Berrier, Bobby L.; and Re, Richard J.: A Review of Thrust-Vectoring Schemes for Fighter Applications. AIAA Paper No. 78-1023, July 1978.

9. Corson, Blake W.; and Runckle, Jack F., Jr.: Calibration of the Langley 16-Foot Transonic Tunnel with Test Suction Air Removal. NASA TR R-423, 1974.

10. Leavitt, Laurence D.: Effect of Empennage Location on Twin-Engine Afterbody/Nozzle Aerodynamic Characteristics at Mach Numbers From 0.6 to 1.2. NASA Technical Report 2116, May 1983.

11. Capone, F. J.: The Nonaxisymmetric Nozzle - It is for Real. AIAA Paper 79-1810, August 1979.

12. Capone, Francis J. and Carson, George T.: Effects of Empennage Surface Loaction on Aerodynamics of a Twin Engine Afterbody Model with Nonaxisymmetric nozzles. NASA Technical Paper 2392. February 1985.

13. Pendergraft, Odis C. Jr.; Burley, James R.; and Bare, E. Ann: Parametric Study of Afterbody/Nozzle Drag on Twin Two-Dimensional Convergent-Divergent Nozzles at Mach Numbers from 0.60 to 1.20. NASA Technical Paper 2640, October 1986.

14. Bangert, Linda S., Leavitt, Laurence D., and Reubush, David E.: Effects of Afterbody Boattail Design and Empennage Arrangement on Aeropropulsive Characteristics of a Twin-Engine Fighter Model at Transonic Speeds. NASA Technical Paper 2704, June 1987.

15. Putnam, Lawrence E.; and Bissinger, N. C.: Results of AGARD Assessment of Prediction Capabilities for Nozzle Afterbody Flows. AIAA - 85-1464, July 1985.

16. Henderson, William P.; and Burley, James R. II: Effect of Empennage Arrangement on Single-Engine Nozzle/Afterbody Static Pressures at Transonic Speeds. NASA Technical Paper 2753, November 1987.

17. Berrier, Bobby L.; and Mason, Mary L.: A Static Investigation of Yaw Vectoring Concepts on Two-Dimensional Convergent-Divergent Nozzles. AIAA Paper 83-1288, June 1983.

18. Berrier, B. L.; and Mason, M. L.: Static Investigation of Post-Exit Vanes for Multiaxis Thrust Vectoring. AIAA Paper 87-1834, June 1987.

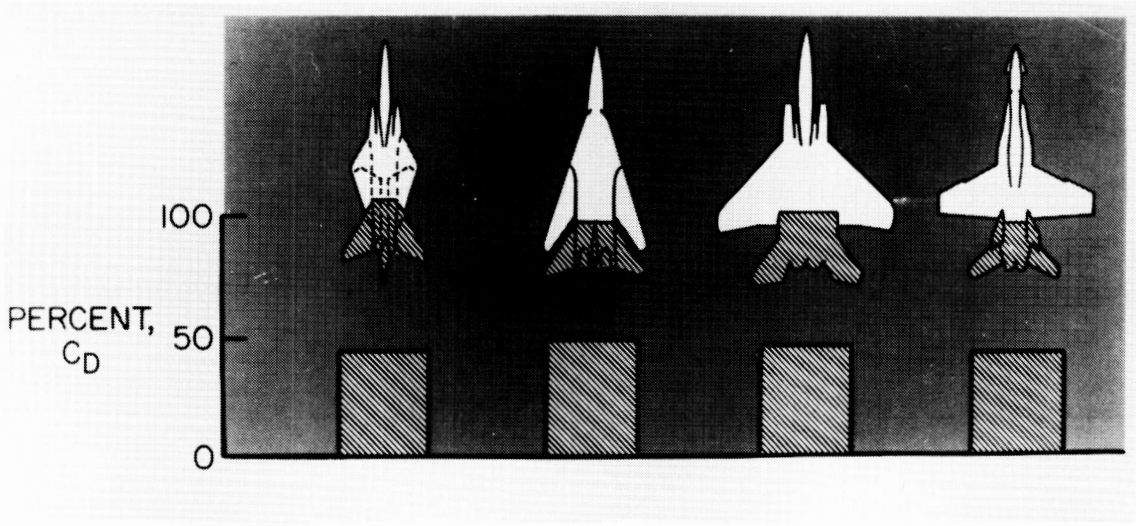

Figure 1. Nozzle/afterbody/empennage drag for high-performance aircraft.

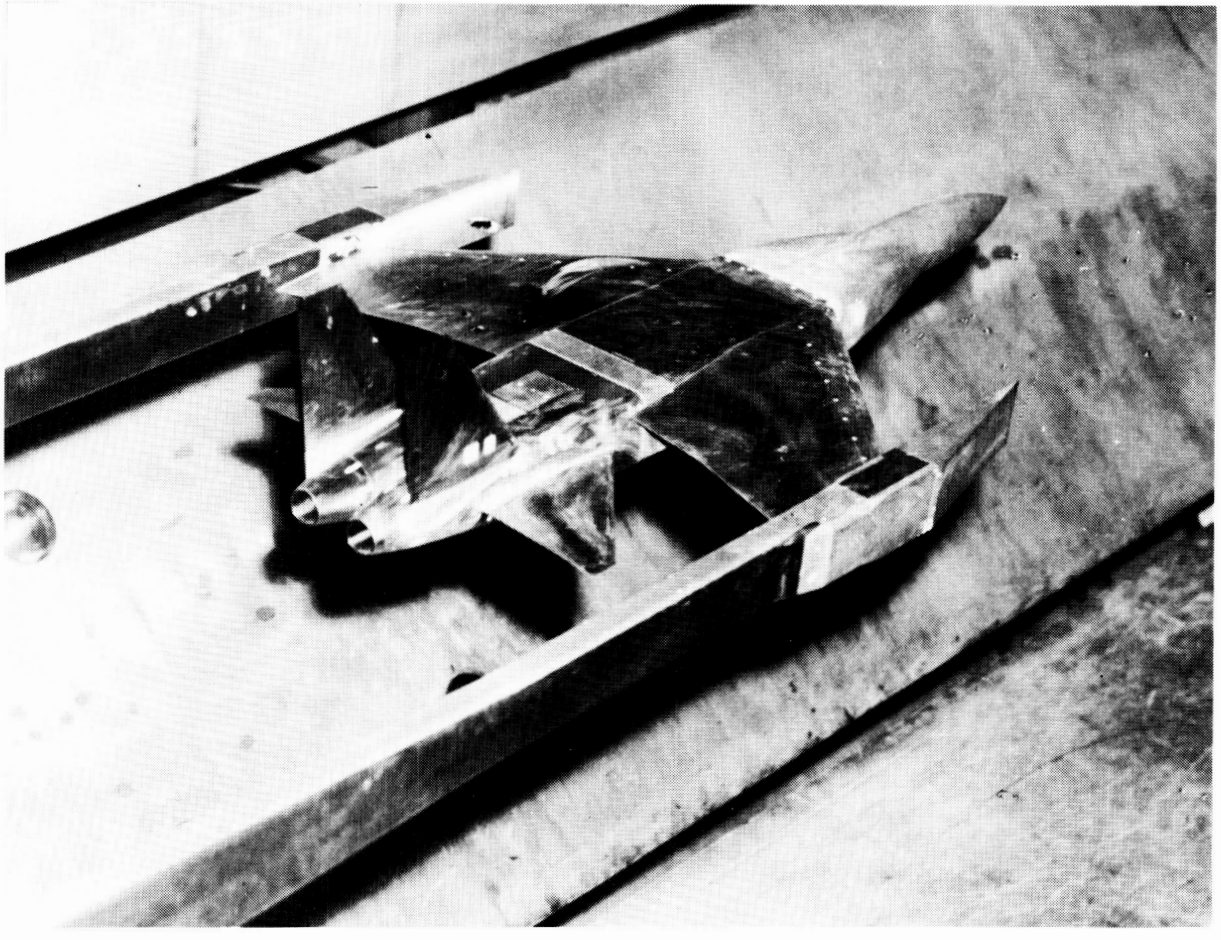

Figure 2. Model with twin axisymmetric nozzles.

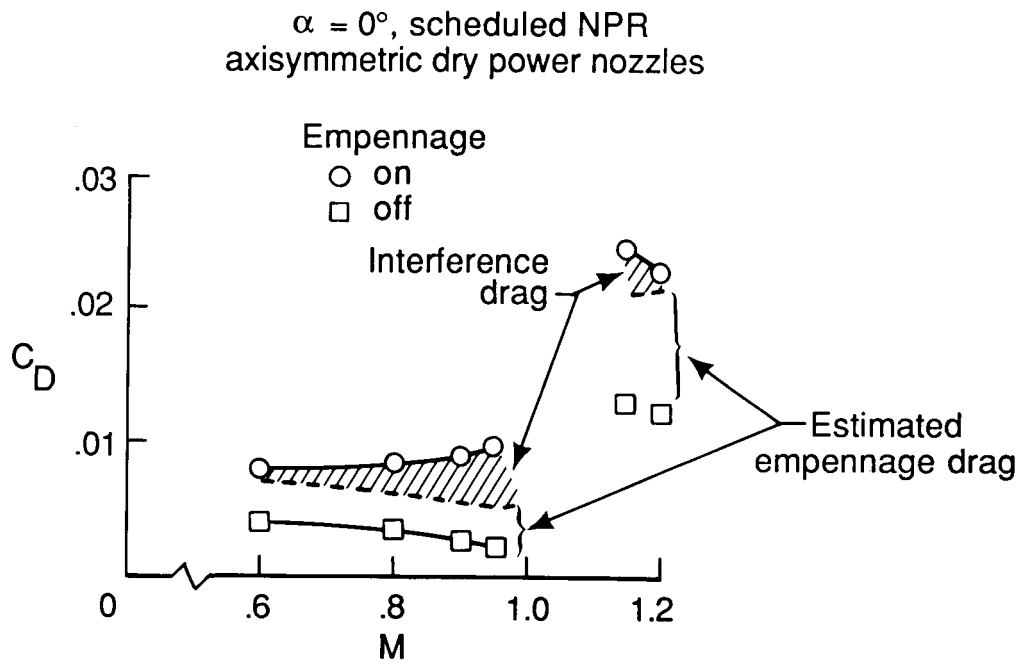

Figure 3. Nozzle/afterbody/empennage drag breakdown.

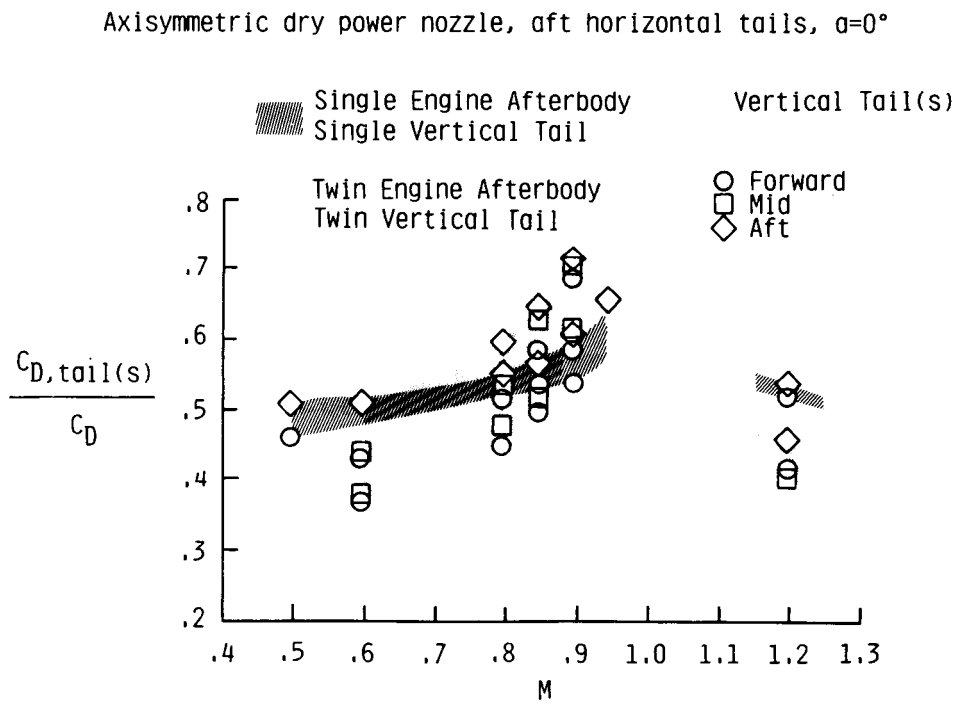

Figure 4. Ratio of tail drag to afterbody drag.

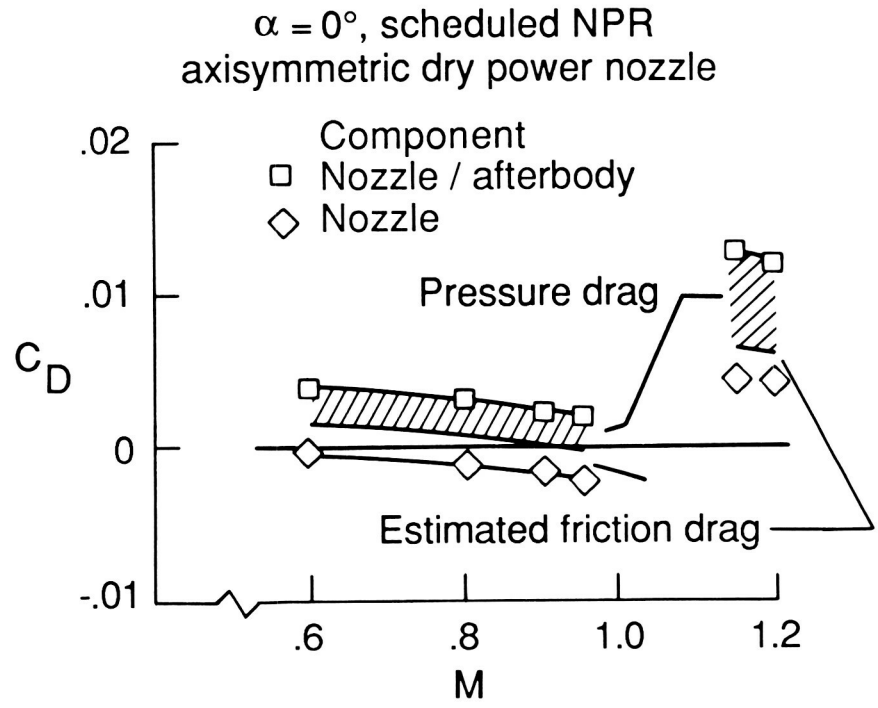

Figure 5. Nozzle/afterbody drag breakdown.

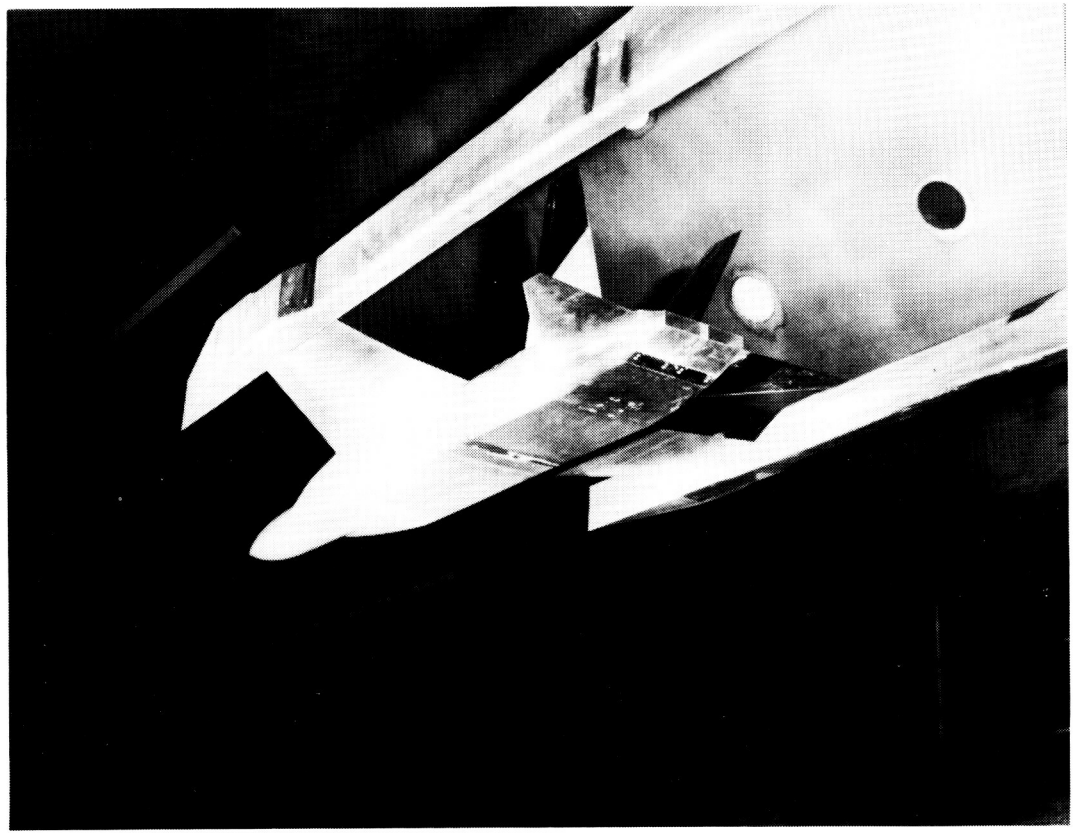

Figure 6. Model with twin nonaxisymmetric nozzles.

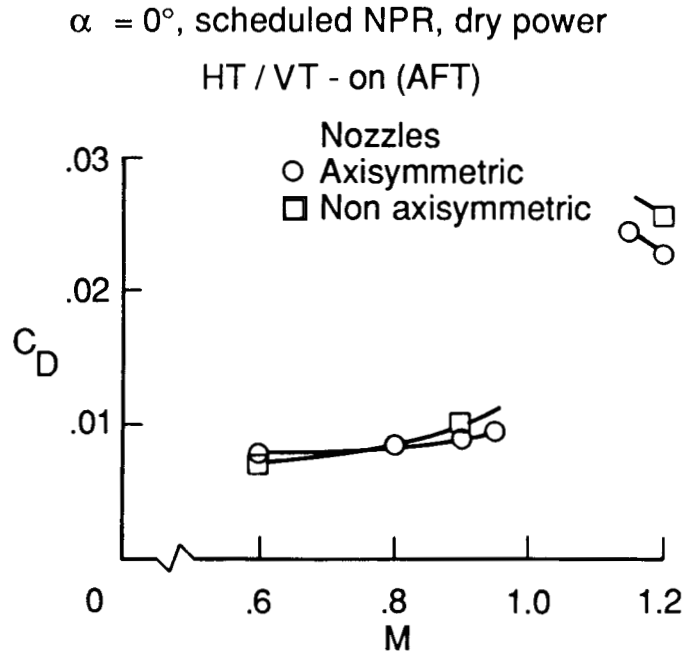

Figure 7. Drag comparison for model with empennage and various nozzle types.

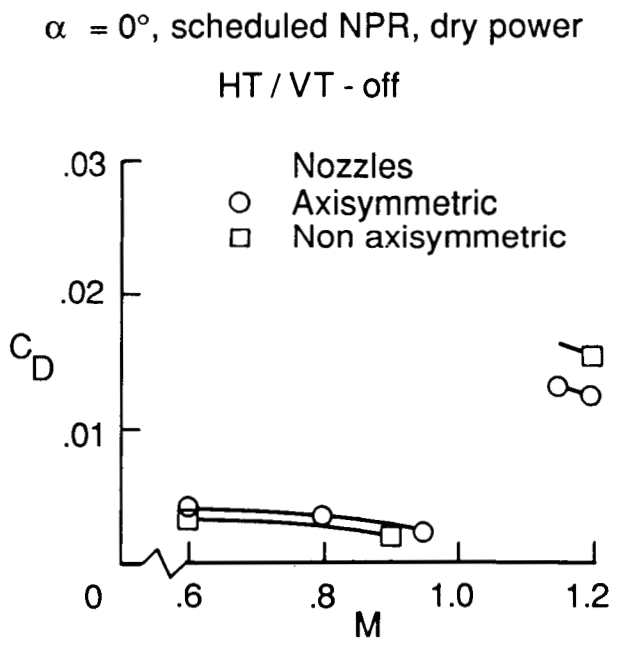

Figure 8. Drag comparison for model without empennage and various nozzle types.

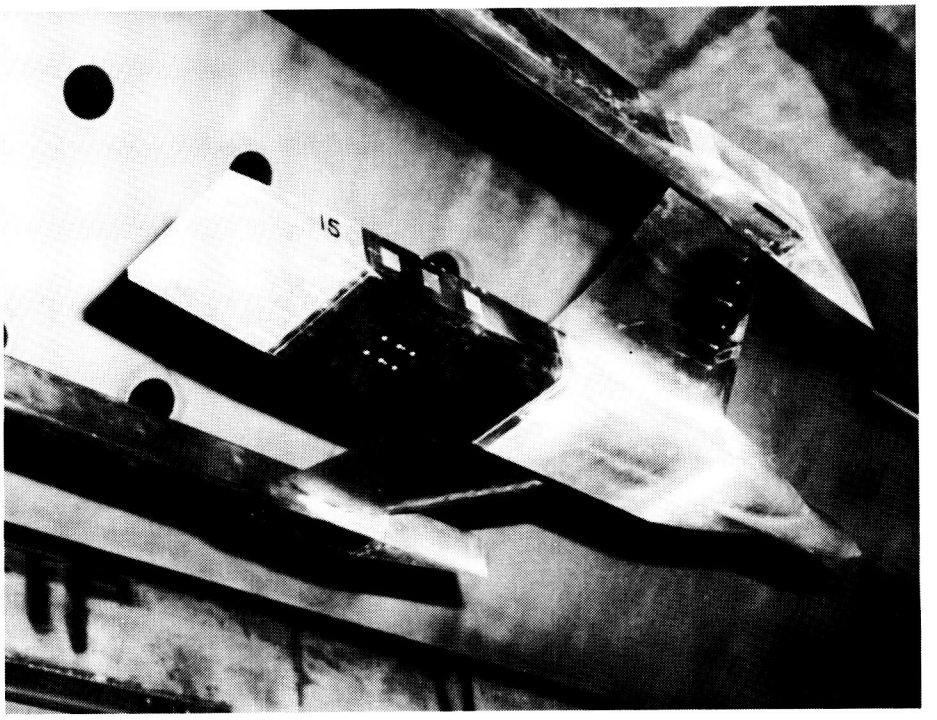

Figure 9. Model with 7.5° boattail nonaxisymmetric nozzles.

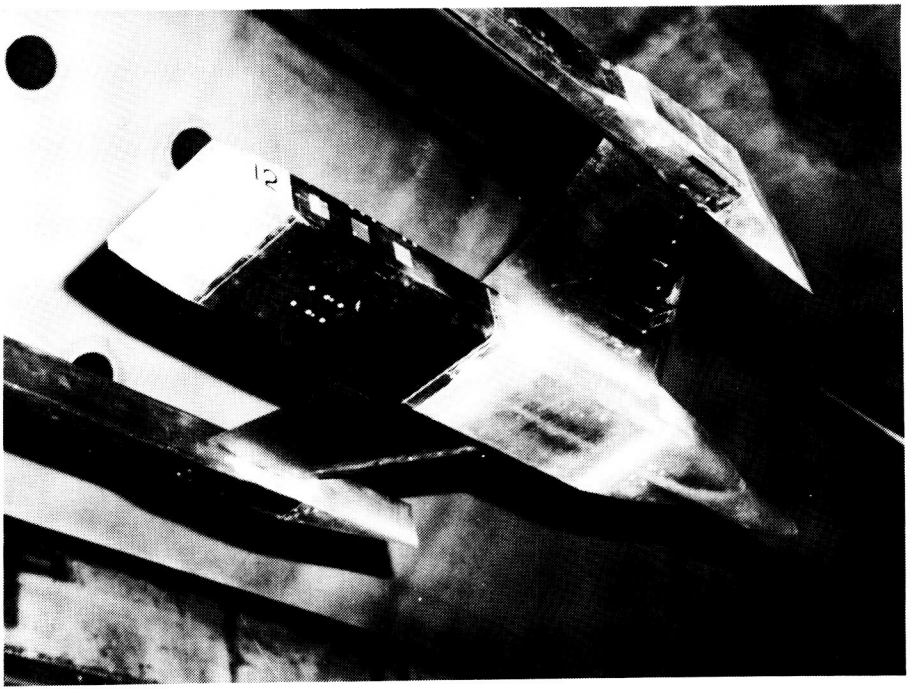

Figure 10. Model with 12.5° boattail nonaxisymmetric nozzles.

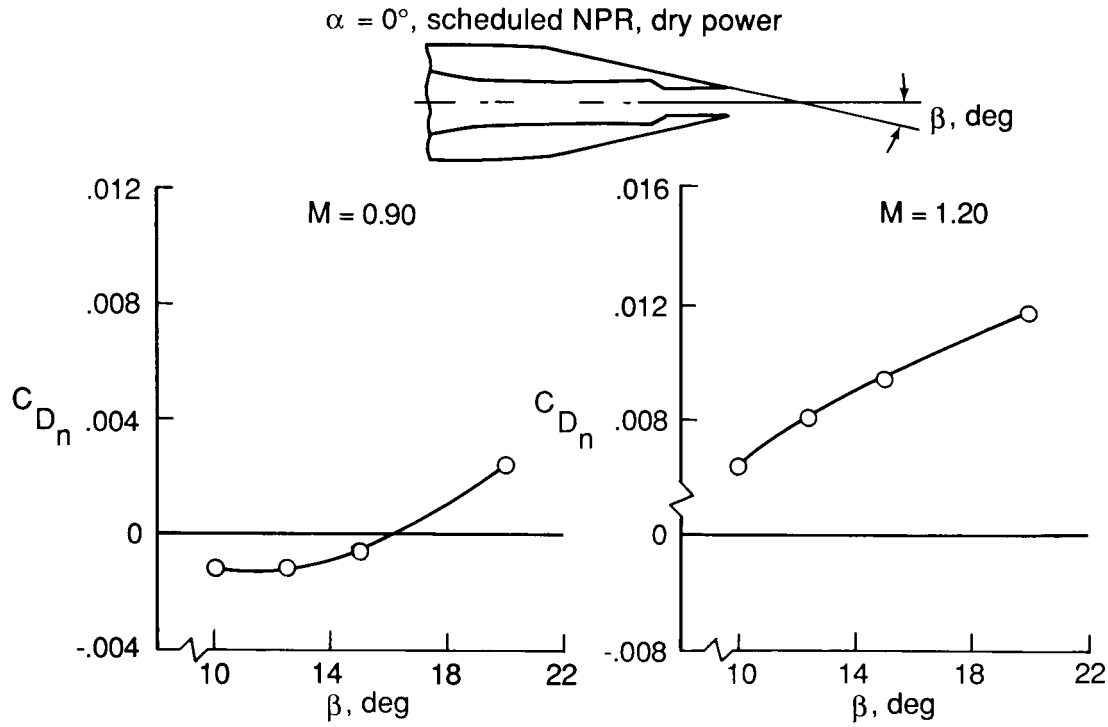

Figure 11. Effect of nozzle boattail angle on nozzle drag.

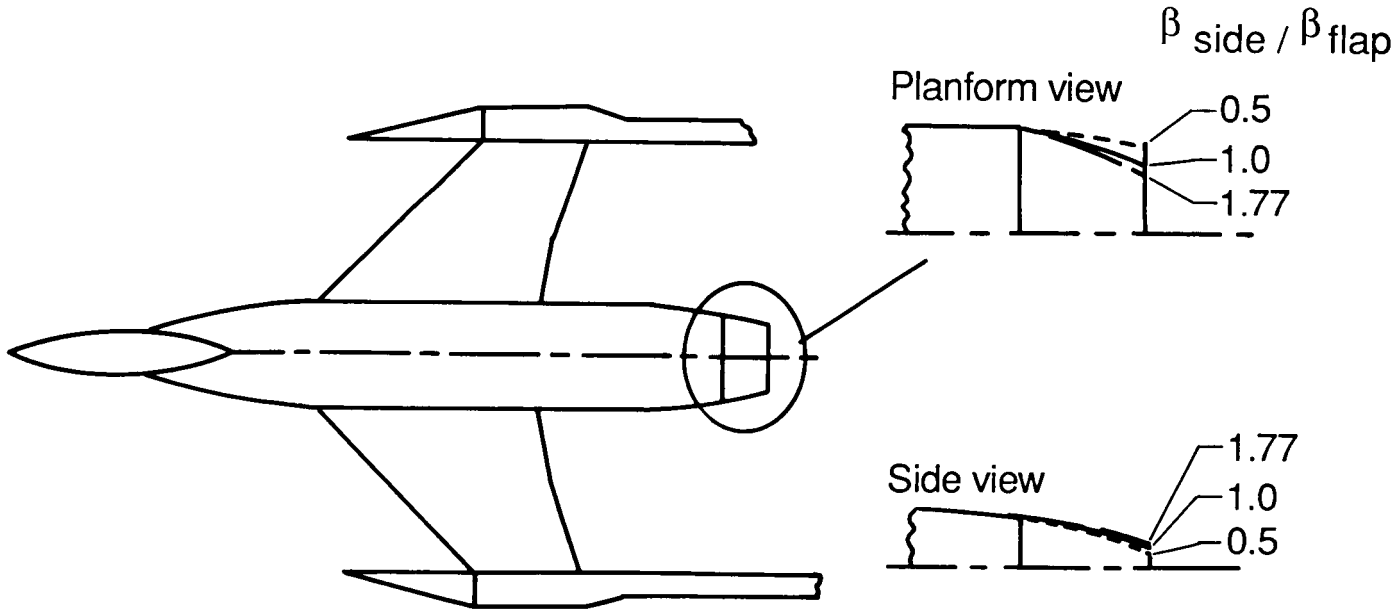

Figure 12. Model showing nozzle boattail angle trade study.

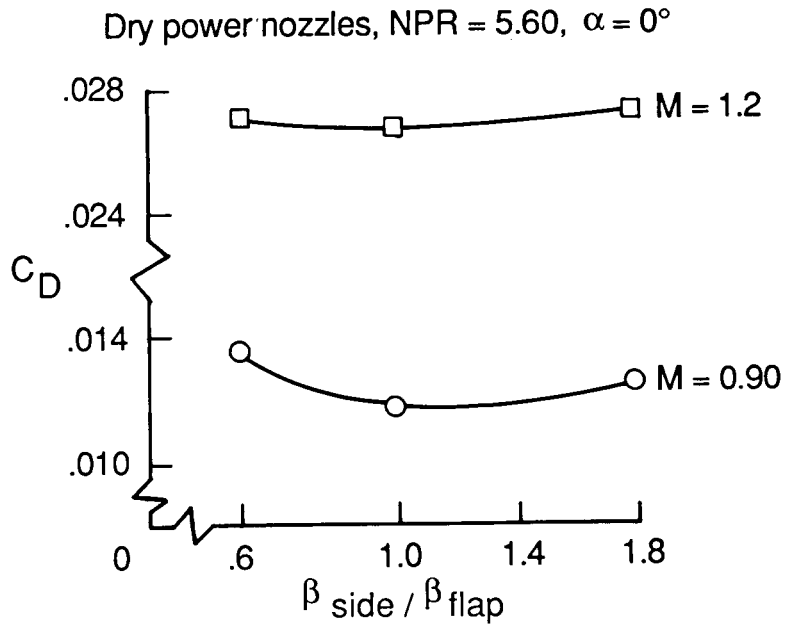

Figure 13. Effect of nozzle sidewall vs. upper/lower flap boattail angle.

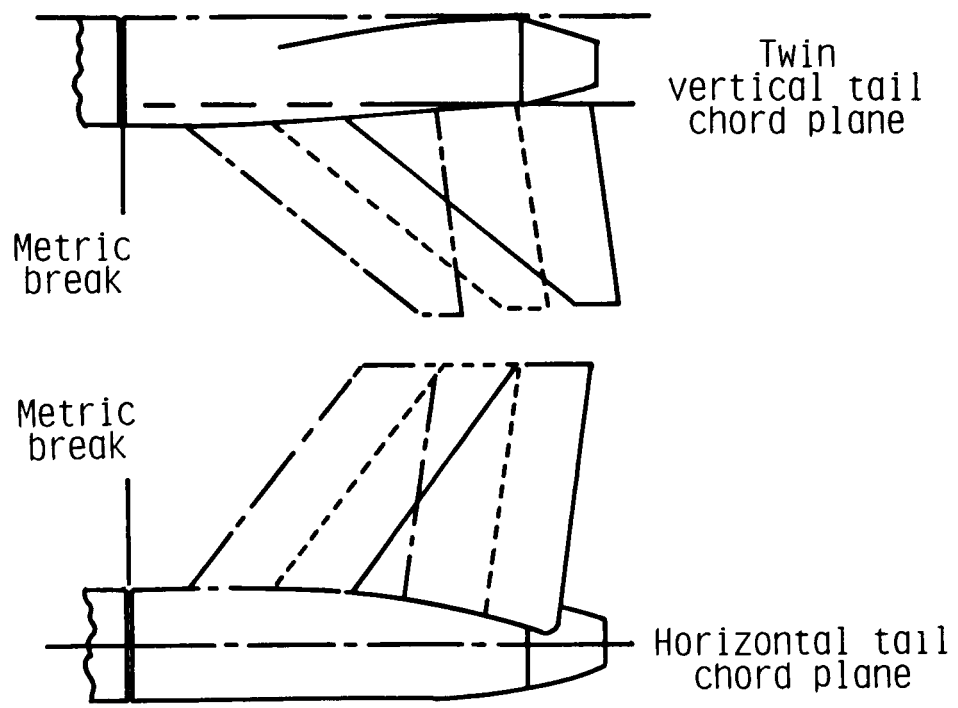

Figure 14. Empennage locations on fuselage.

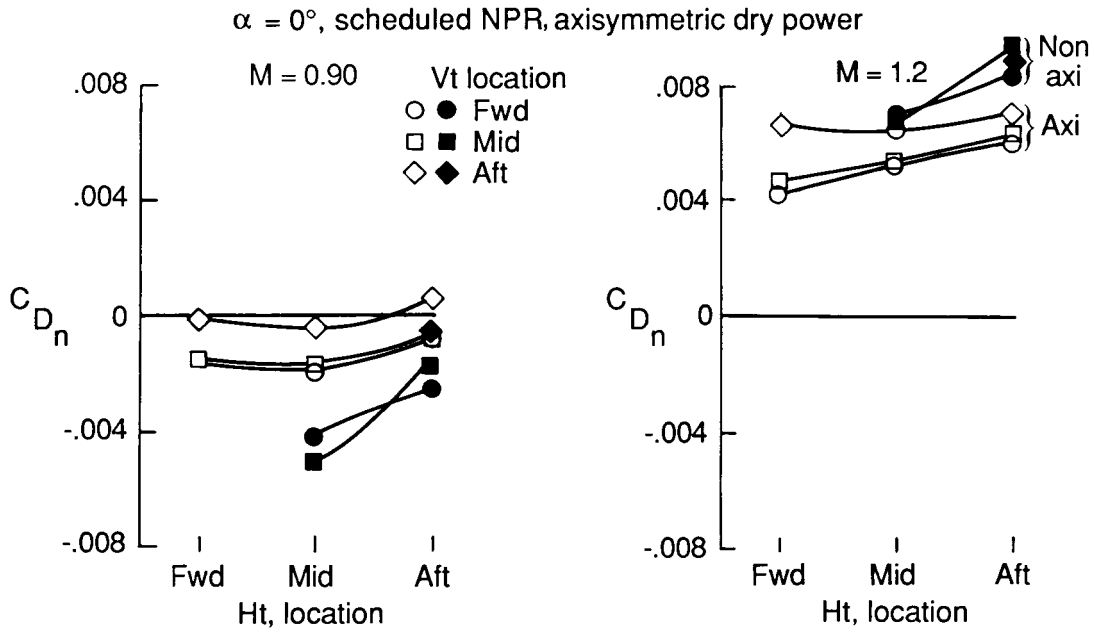

Figure 15. Effect of horizontal and vertical tails on nozzle drag.

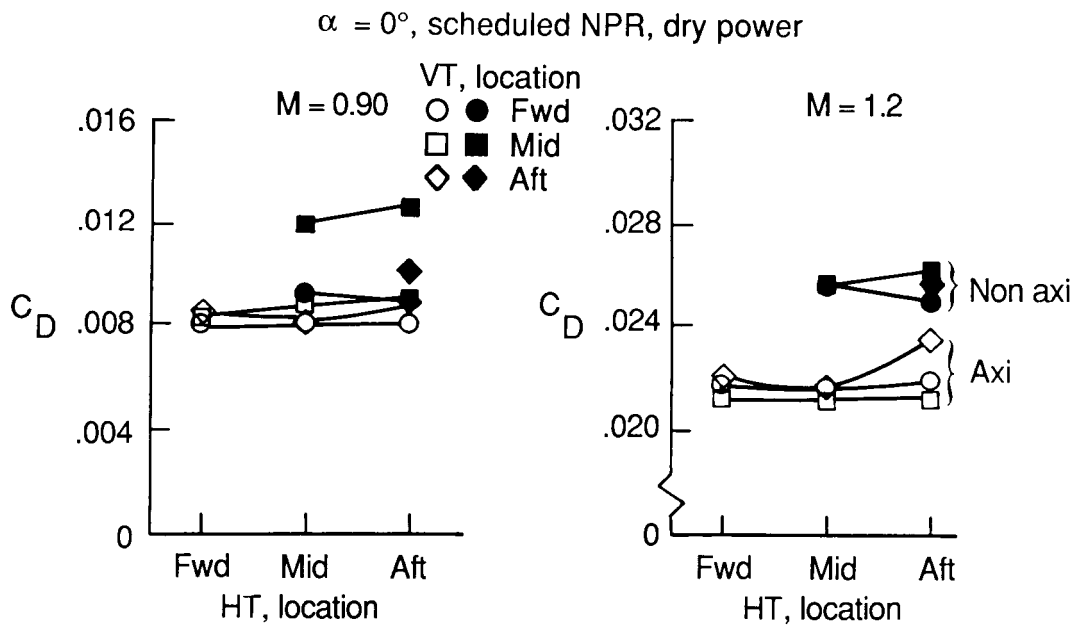

Figure 16. Effect of horizontal and vertical tails on total nozzle/afterbody drag.

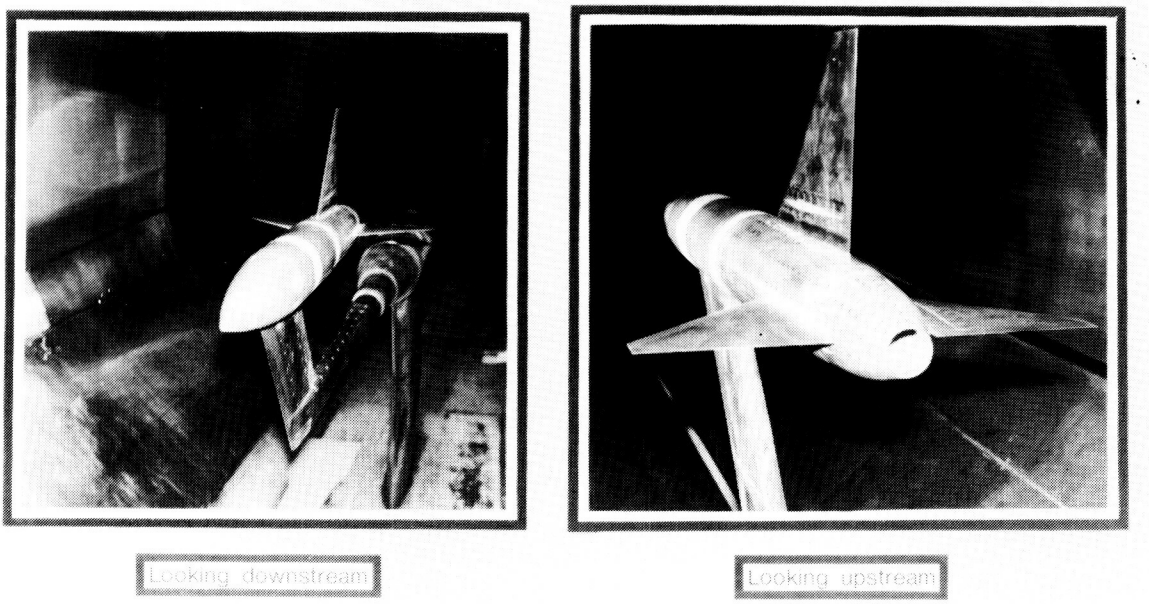

Figure 17. Model installed in the 16-Foot Transonic Tunnel.

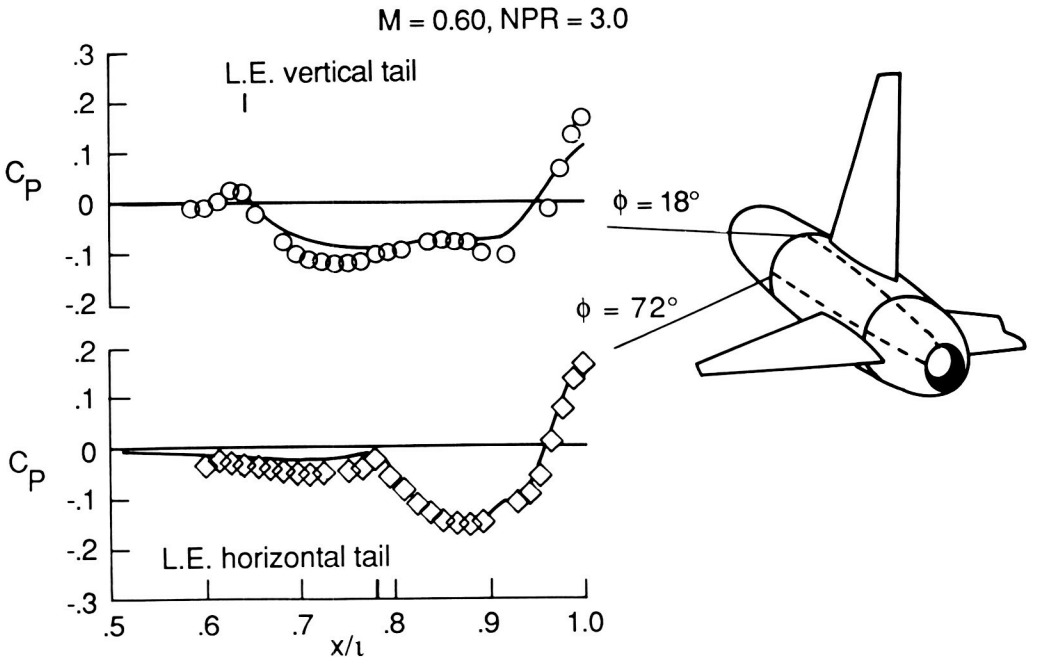

Figure 18. Comparison of experimental and theoretical pressure coefficients at M = 0.60.

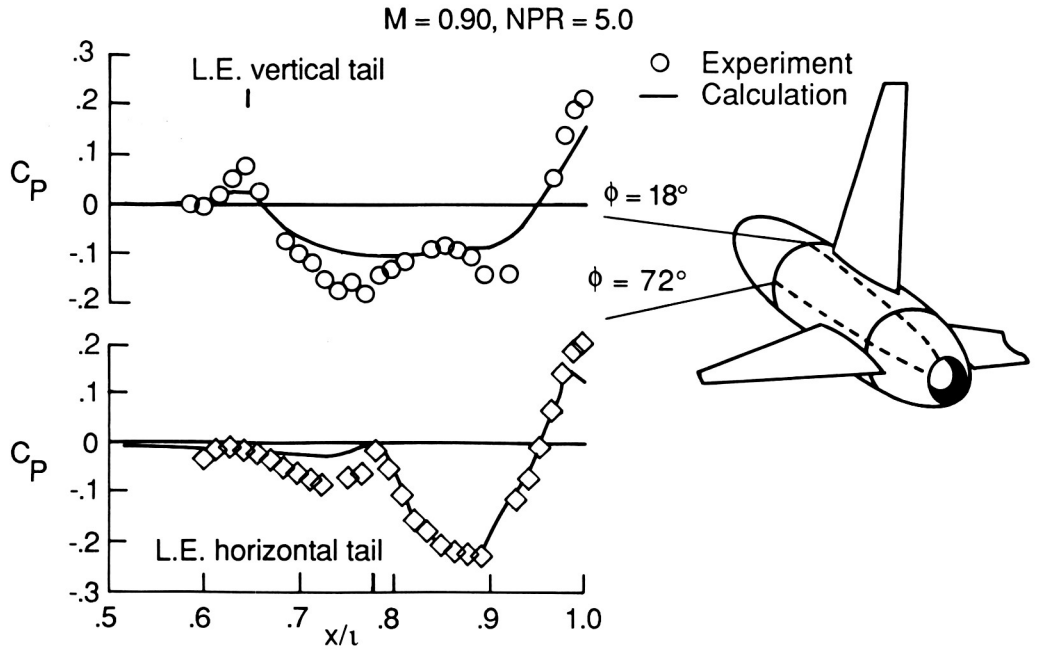

Figure 19. Comparison of experimental and theoretical pressure coefficients at M = 0.90.

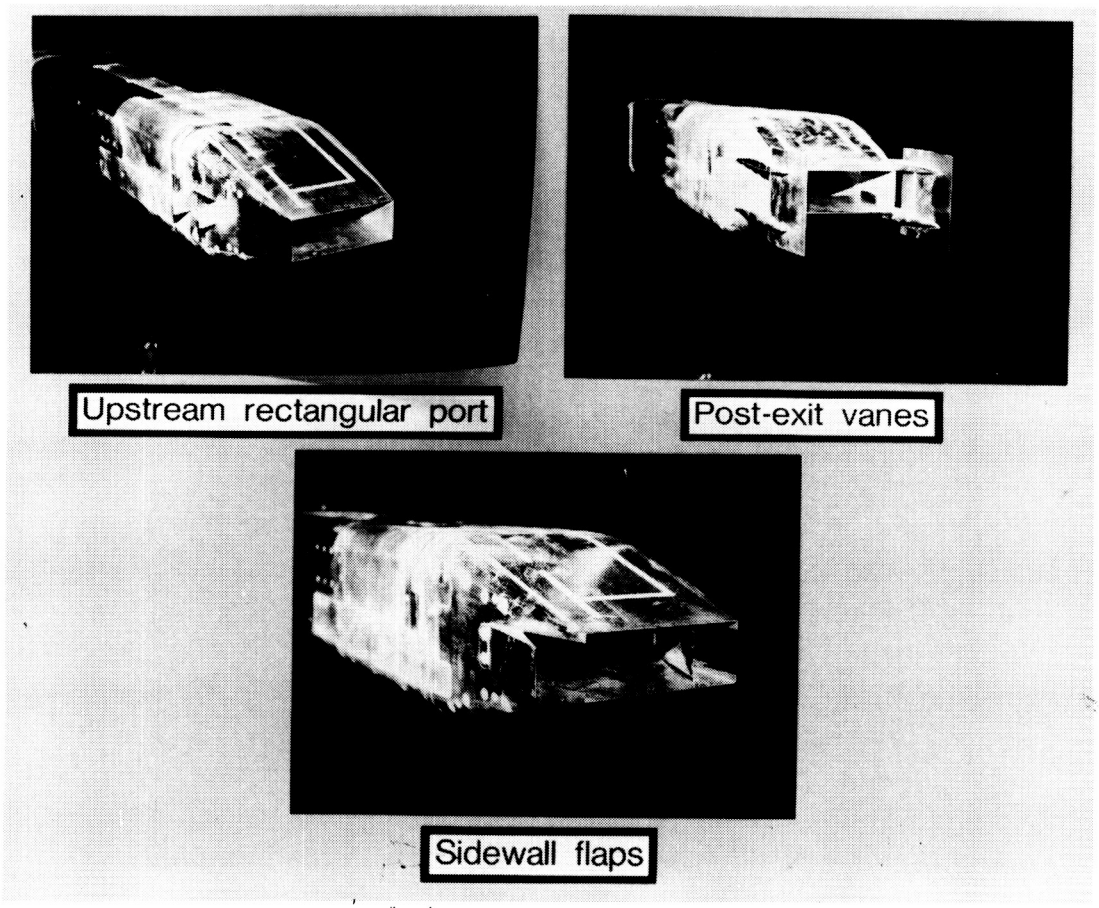

Figure 20. Yaw vector concepts.

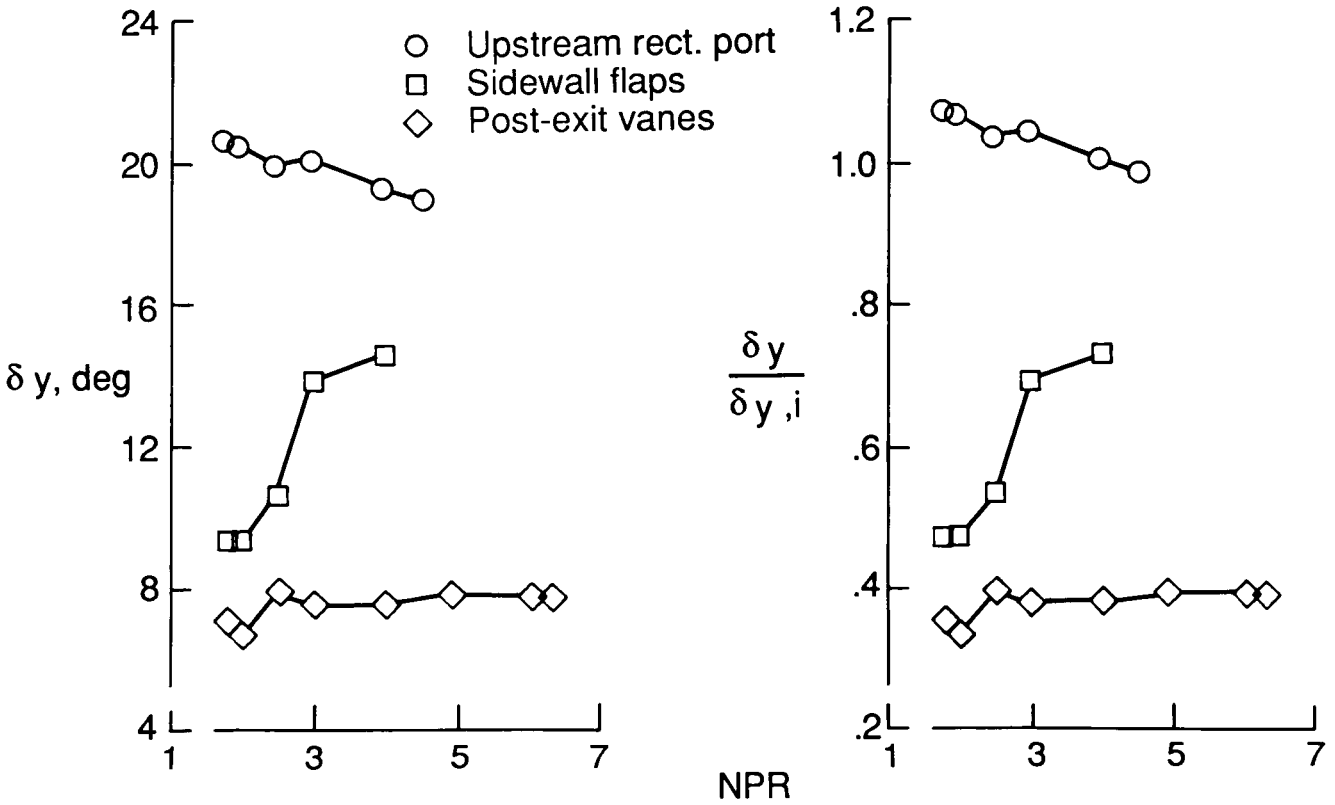

Figure 21. Flow turning performance of yaw vector concepts at M = 0.0.

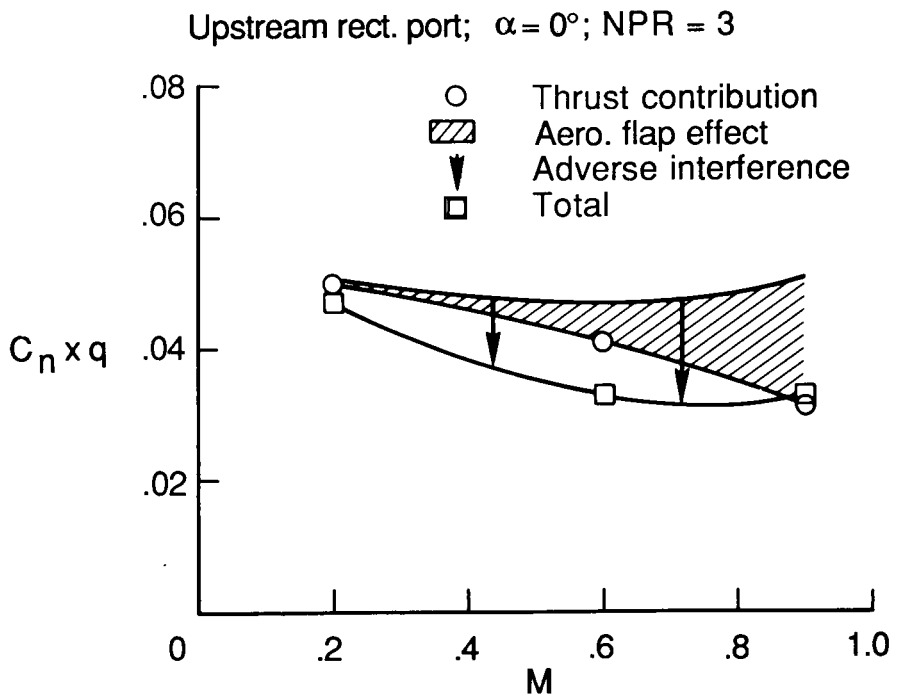

Figure 22. External flow effects on vectored thrust yawing moment for upstream rectangular port model.

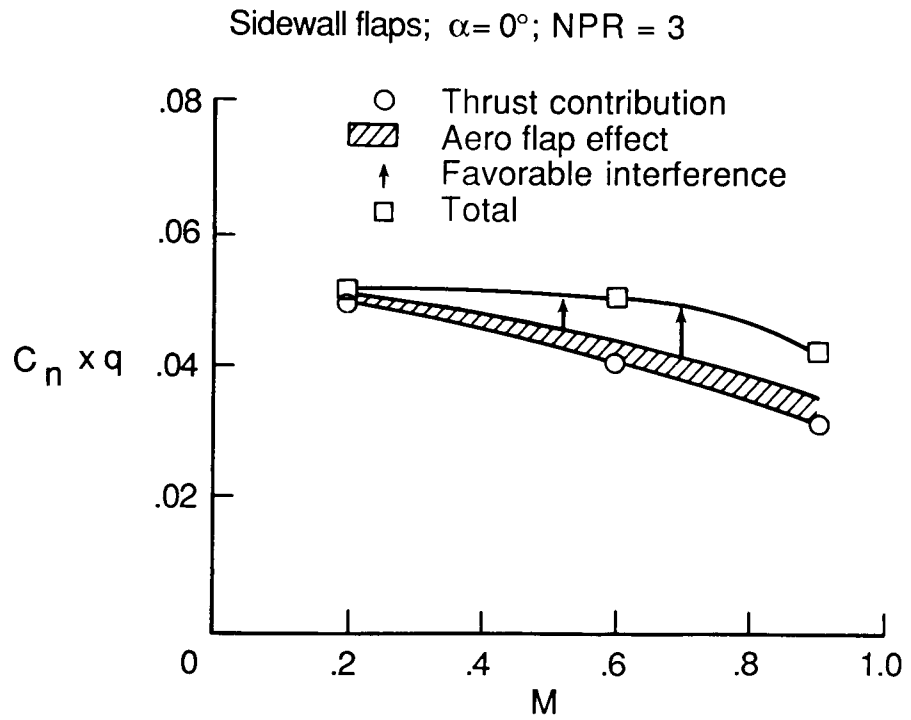

Figure 23. External flow effects on vectored thrust yawing moment for model with sidewall flaps.

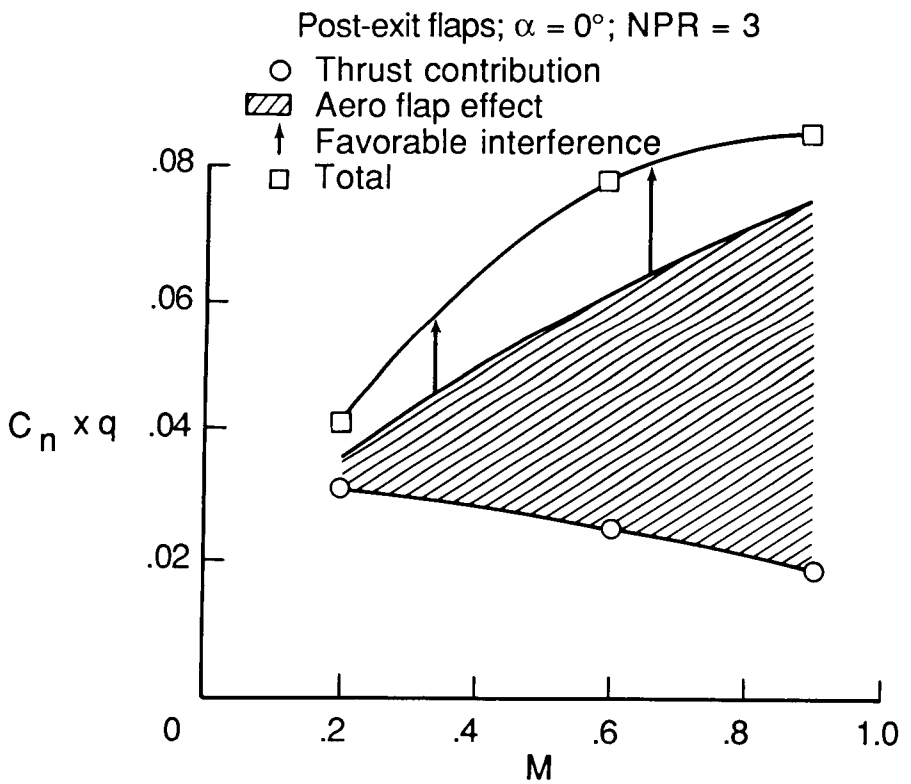

Figure 24. External flow effects on vectored thrust yawing moment for model with post-exit flaps.

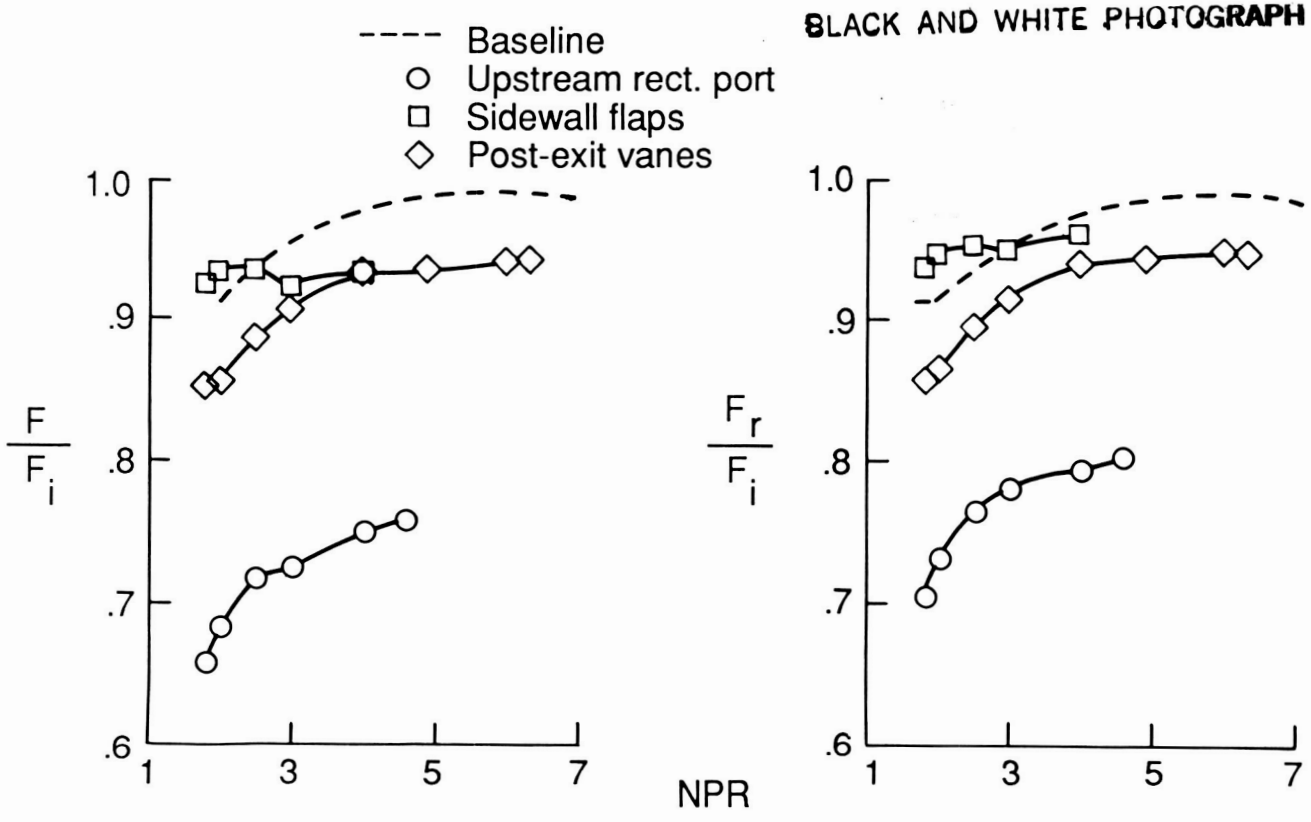

Figure 25. Thrust performance of yaw vector concepts at M = 0.0.

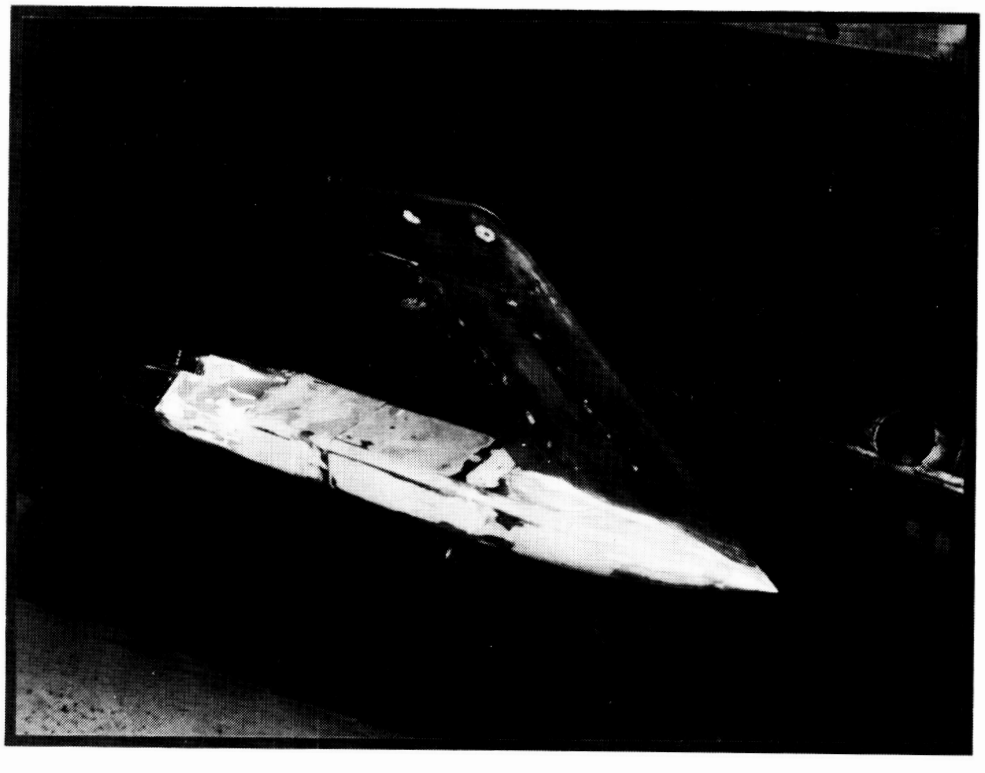

Figure 26. Model with canted nozzles in the 16-Foot Transonic Tunnel.

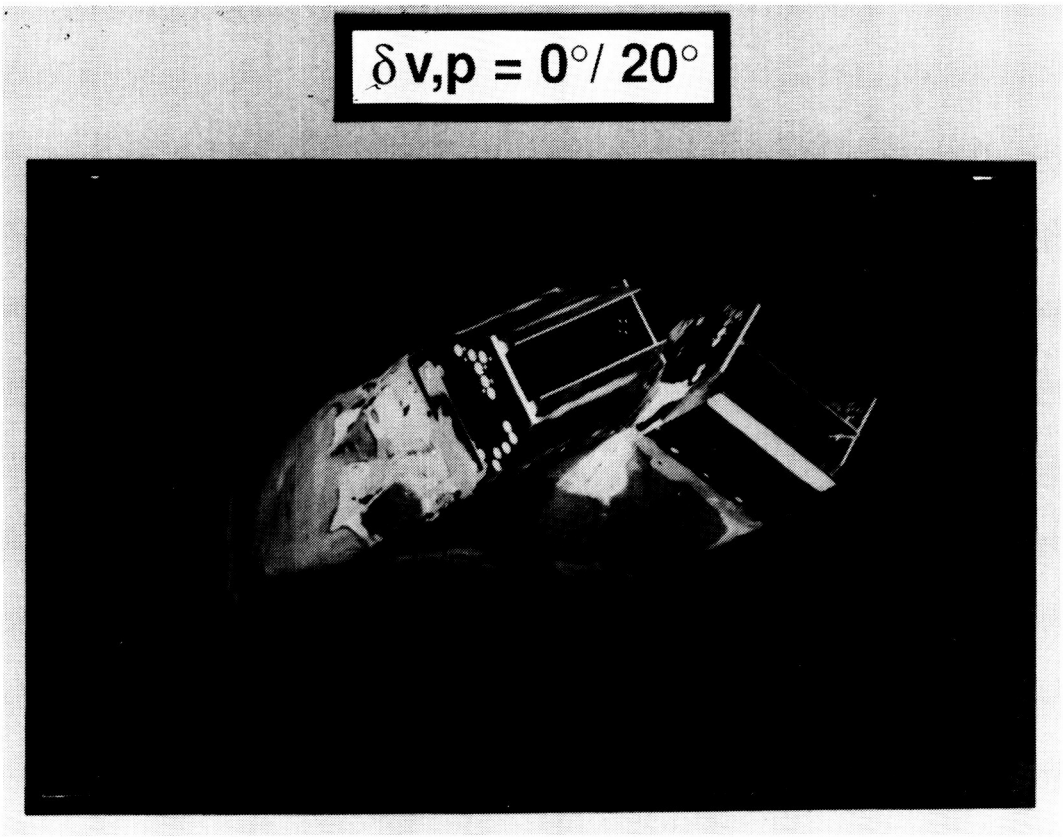

Figure 27. Model with nozzles canted 30°.

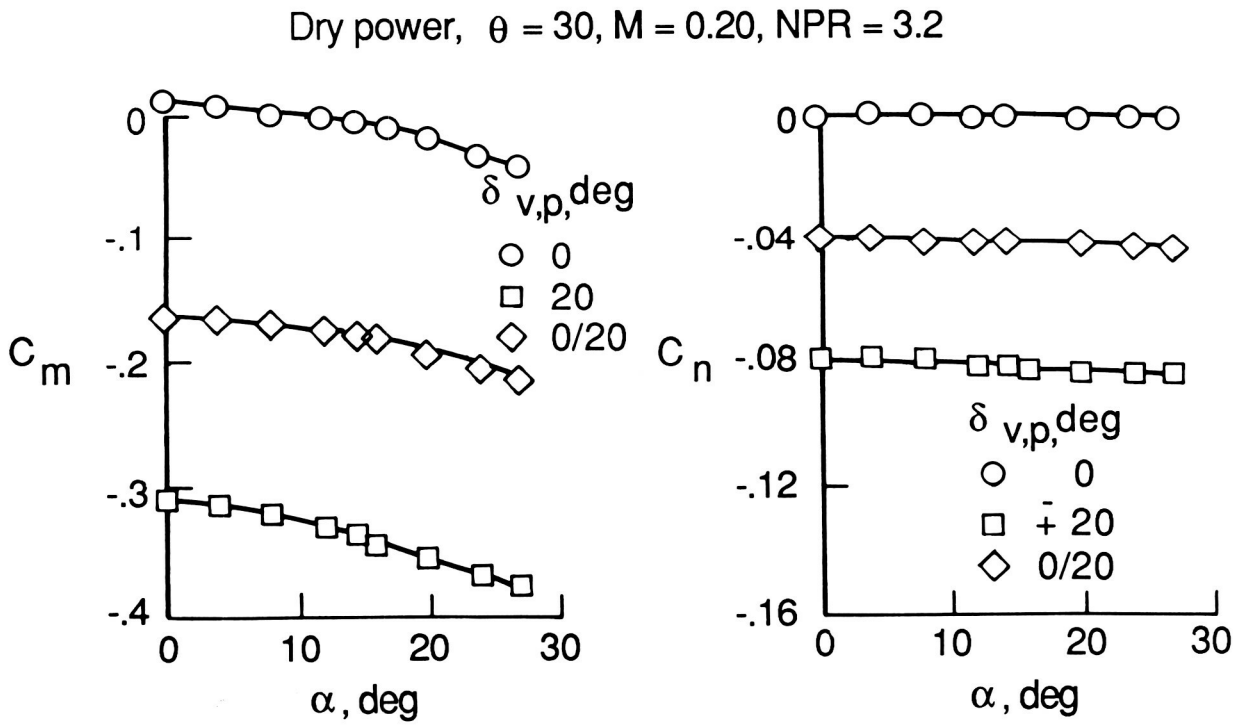

Figure 28. Effect of nozzle flap deflection on pitching and yawing moments.

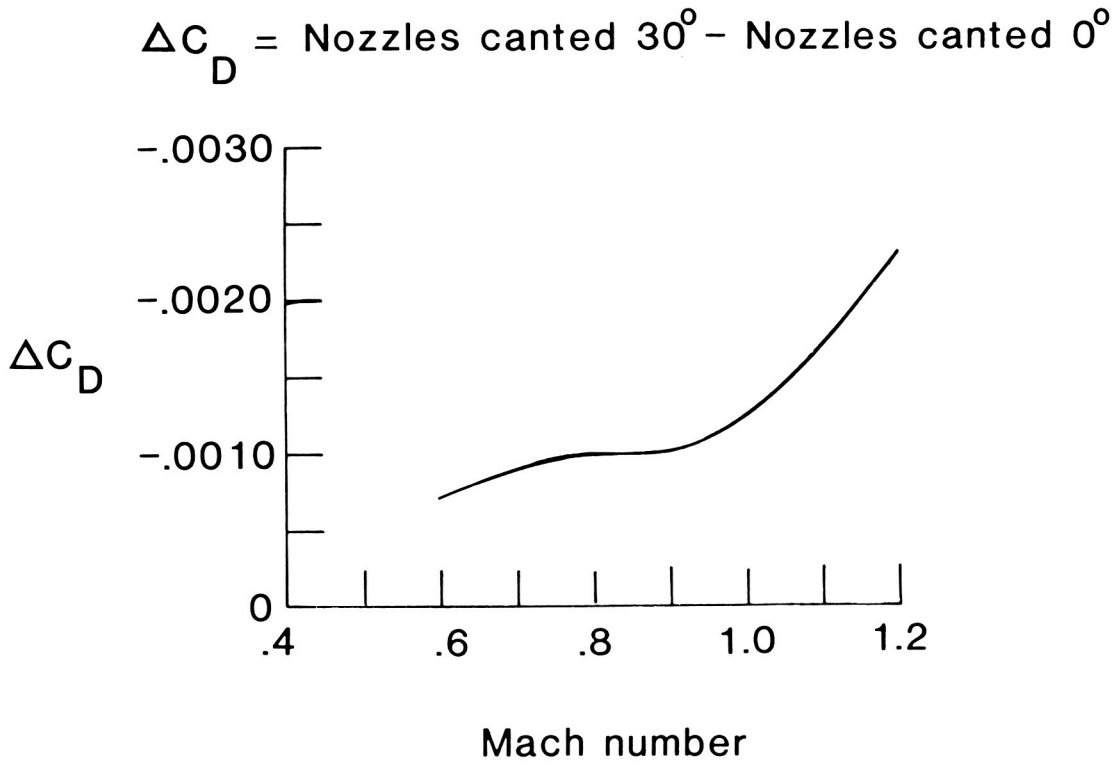

Figure 29. Drag reduction due to canted nozzles.

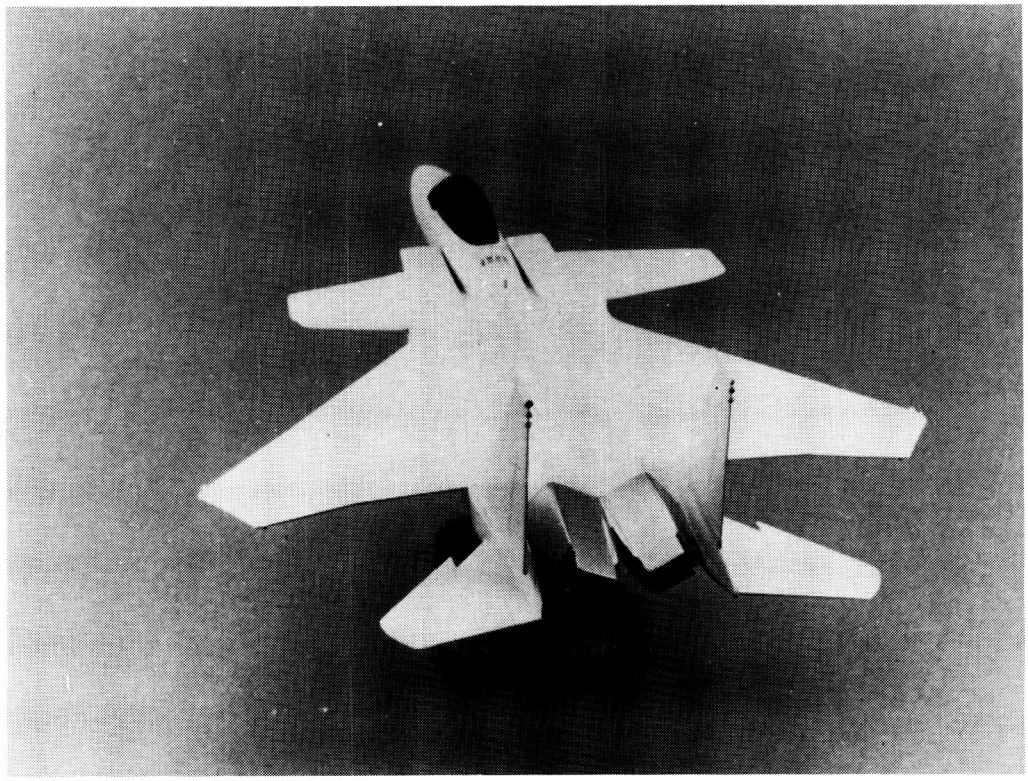

Figure 30. Top view of the F-15 SMTD with canted nozzles.

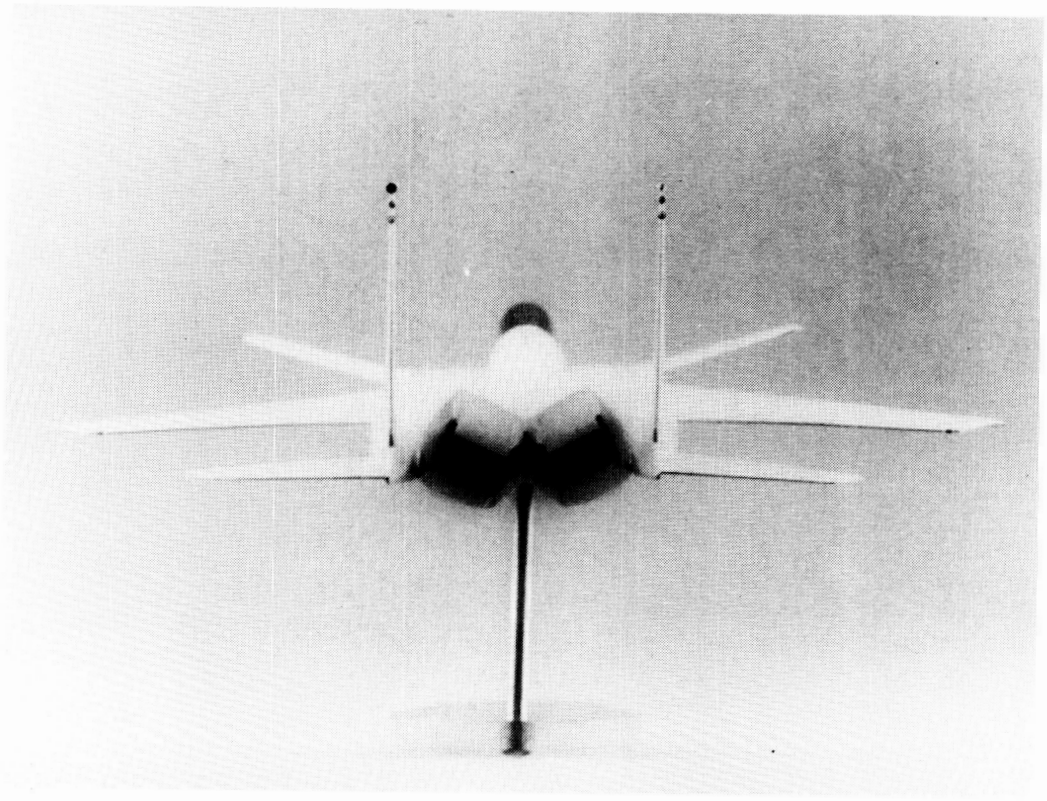

Figure 31. Rear view of the F-15 SMTD with canted nozzles.